



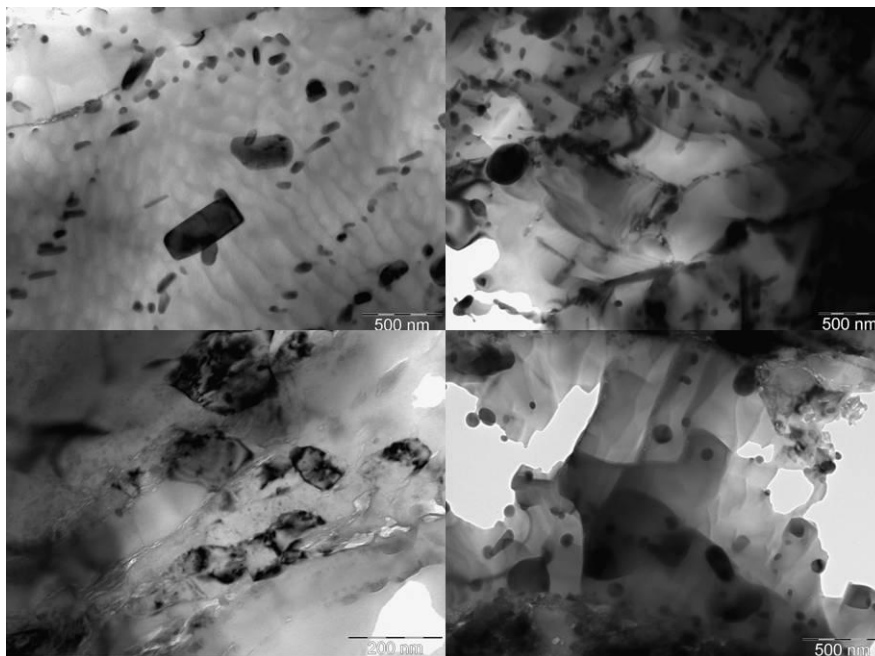
UNIVERSITY
OF TRENTO - Italy

Department of Materials Engineering
and Industrial Technologies

Doctoral School in Materials Engineering – XXIII cycle

Cryomilling and Spark Plasma Sintering of 2024 Aluminium Alloy

Kétner Bendo Demétrio



April 2011

CRYOMILLING AND SPARK PLASMA SINTERING OF 2024 ALUMINIUM ALLOY

Kétner Bendo Demétrio

Tutor:

Prof. Alberto Molinari

Doctoral Committee:

Prof. Gian Domenico Soraru' – Università degli Studi di Trento

Prof. Hebert Danninger – Vienna University of Technology

Prof. Michel Vert – Université de Montpellier I

Prof. Laura Montanaro – Politecnico di Torino

29th April 2011

*To my parents
Valmir and Maria do Carmo*

INDEX

INTRODUCTION	7
References	11
CRYOMILLING AND MICROSTRUCTURAL CHARACTERIZATION OF THE 2024 ALUMINIUM ALLOW POWDER	14
1.1 Mechanical Milling	14
1.1.1 <i>The Formation of the Nanostructure on Milling</i>	18
1.1.2 <i>Minimum Grain Size Obtainable by Milling</i>	19
1.1.3 <i>Cryogenic Milling</i>	22
1.2 Experimental Procedures	23
1.2.1 <i>Cryogenic Milling</i>	23
1.2.2 <i>Powder Characterization</i>	24
1.3 Results and Discussion	26
1.3.1 <i>Cryomilling with BPR 4:1</i>	26
1.3.1.1 <i>Characterization of the Cryomilled Powder</i>	26
1.3.1.2 <i>Thermal Stability of the Cryomilled Powder</i>	29
1.3.1.3 <i>Incoherent Precipitation on Ageing of the Cryomilled Powder</i>	33
1.3.2 <i>Cryomilling with BPR 32:1</i>	37
1.3.2.1 <i>Characterization of the Cryomilled Powder</i>	37
1.3.2.2 <i>Thermal Stability of the Cryomilled Powder</i>	39
1.3.2.3 <i>Transformation on Heating of the Cryomilled Powder</i>	41
1.3.2.4 <i>Degassing of the Cryomilled Powder</i>	43
1.3.2.5 <i>Transformation on Heating of Cryomilled and Degassed Powder..</i>	45
1.4 Summary	48

References	50
SINTERING OF THE BIMODAL ULTRA-FINE GRAINED/MICROMETRIC POWDERS BY SPARK PLASMA SINTERING	53
2.1 Spark Plasma Sintering	53
2.2 Experimental Procedures	56
2.2.1 Spark Plasma Sintering	56
2.2.2 Characterization of the Sintered Samples	56
2.3 Results and Discussion	58
2.3.1 Cryomilling with BPR 4:1	58
2.3.1.1 Densification of the Powder	58
2.3.2 Cryomilling with BPR 32:1	60
2.3.2.1 Densification of the Powder	61
2.3.2.2 Impurities in the Sintered Sample	63
2.3.2.3 Characterization of the Sintered Sample	64
2.4 Summary	72
References	73
HOT DEFORMATION BEHAVIOUR OF THE BIMODAL ULTRA-FINE GRAINED/MICROMETRIC ALLOY	75
3.1 Hot Workability	75
3.1.1 Strain Rate Sensitivity	77
3.1.2 Processing Map	78
3.2 Experimental Procedures	82
3.2.1 Hot Deformation Tests	82
3.2.2 Microstructural Characterization	83
3.3 Results and Discussion	84
3.3.1 Hot Deformation of Atomized Sintered Alloy	84
3.3.1.1 Relative Work Softening	88
3.3.1.2 Strain Rate Sensitivity	89

Index

3.3.1.3	<i>Processing Map</i>	90
3.3.1.4	<i>Instability Map</i>	92
3.3.2	<i>Hot Deformation of Milled Sintered Alloy</i>	95
3.3.2.1	<i>Relative Work Softening</i>	99
3.3.2.2	<i>Strain Rate Sensitivity</i>	100
3.3.2.3	<i>Processing Map</i>	101
3.3.2.4	<i>Instability Map</i>	102
3.3.3	<i>Comparison Between Atomized and Milled Alloys</i>	107
3.3.3.1	<i>Flow Stress Behaviour</i>	107
3.3.3.2	<i>Microstructural Characterization</i>	112
3.4	Summary	119
	References	121
CONCLUSIONS		124
	References	126
ACKNOLODGMET		127
PUBLICATIONS		128

INTRODUCTION

Aluminium alloys are characterized by a low specific weight, which make them highly interesting for structural applications. Mechanical properties are lower than those of steels, so the possibility to obtain an increase by means of the structural refining (either nano- or ultra-fine grained structure) would extend their applications in several fields.

Bulk nanocrystalline metals and alloys can be produced by high energy milling of powders and their consolidation by sintering techniques characterized by a low thermal load in order to minimize grain growth. This is an alternative approach to other methods based on severe plastic deformation, with the advantage of obtaining near-net shape parts, within the limits of the Powder Metallurgy (PM) route. Even in the case of the part cannot be obtained directly a preform can be produced by Powder Metallurgy and finished by hot working. In this case, Powder Metallurgy is used to produce preforms with geometry closer to the final one than that attainable by other technologies, reducing production costs and raw material consumption.

It is well known that nanostructure ($D < 100$ nm) of Al alloys can be obtained by high energy milling technique (1) (2). During milling, the grain size is determined by equilibrium between recovery and formation of

defects due to heavy plastic deformation (3). Face centered cubic (FCC) materials, as Al and alloys, are difficult to reduce by mechanical milling. The opposite occurs with body centred cubic (BCC) and hexagonal close packed (HCP) metals due to relatively defects accumulation and difficult of fast recovery kinetics (4) (5).

A valid alternative is the cryogenic milling, where the powders are milled in slurry formed with liquid nitrogen (1) (6). Cryomilling takes advantage due to low temperature of the liquid nitrogen that either suppresses or limits recovery and recrystallization and leads to finer grain structure faster (7) (8). In addition cryogenic milling does not require use of process control agent (PCA) that can contaminate the powder with carbon and oxygen (1). A very important factor to preserve the nanostructure of a material is its thermal stability that depends on the balance between driving and resisting forces. It is well known that the smaller the grain size, the bigger the tendency to grain growth. In most cases, the thermal stability of a nanostructure depends on the lattice defects stored between and within grains, and on the particles such as nitrides and oxides precipitated at the grain boundaries (9) (10) (11). It is really important achieve an equilibrium between grain size and thermal stability of the material to avoid grain growth on sintering. Moreover, if the powder particles are very fine, sintering becomes hard because of the oxide layer that surrounds the particles.

Bulk nanomaterials can be produced through several PM techniques. Hot isostatic press (HIP), dynamic consolidation, hot extrusion and spark plasma sintering (SPS) are effective to achieve a full dense material (12) (13) (14). In the frame of the near-net shape technologies, SPS is a novel technology that has large potentiality, because of the lower temperature

and shorter time required (15) (16) (17). In this process a pulse electric current flows directly on the powders and a high heating efficiency is offered.

It is known that Al powders are hardly sinterable due to oxide layer on their surface. This layer has to be broken in order to form a solid neck between the particles (16). SPS has been used to produce nanostructured Al (16) (18) and iron alloys (19) starting from nanostructured powders.

A bimodal microstructure can be formed during SPS sintering due to the localized overheating generated by the sparks and low thermal stability of the material (20). It is well known that a bimodal microstructure reveals an improvement of ductility (21) (22) (23) (24) which is the most critical characteristics of nanostructured metals. In a simplistic view, ultra-fine/nano crystallites are responsible for high strength and micrometric grains provide increased ductility. Additional strategies of ductility improvement provides deformation at low temperatures/high strain rates, which furnishes accumulation of dislocations within nanocrystalline/UFG, resulting in increased strain hardening (25) and enhancement of strain rate sensitivity of the flow stress (26).

Hot workability of metals depends on several parameters. Temperature and strain rate affect the flow stress and the strain rate sensitivity (27). The former increases on decreasing grain size, until the deformation process is determined by dislocation motion. In FCC materials, particularly in Al and its alloys, refining grains to UFG level promotes an increase in strain rate sensitivity (27) (28) (29). The hot workability is usually defined as the quantity of deformation that a material can undergo without cracking and reaching desirable deformed microstructures at a given temperature and strain rate. Improving workability means increasing the processing ability

and the properties of the materials (30) (31). Hot workability can be studied by the approach of the power dissipation maps (32).

In this PhD work, the production of nanometric Al 2024 alloy powder by cryomilling, ultra-fine grained/micrometric material consolidated by SPS, and its further deformability at high temperature was studied. The results are presented in three chapters.

Chapter 1 reports the methodology to obtain the nanostructured 2024 alloy powder. Many aspects such as the evolution of the microstructure, the role of liquid nitrogen during milling and the thermal stability are studied in order to have an insight on the kinetics (1). The study of the thermal stability of the nanostructured powder is presented, as well.

Chapter 2 describes the SPS experiments of the as-atomized and as-milled powders and the characterization of the consolidated material.

Chapter 3 reports the hot compression experiments on the atomized and milled samples, and discusses the differences in the deformation behaviour on the basis of the starting microstructure and of its evolution during deformation.

REFERENCES

- (1) D.B.Witkin, E.J.Lavernia. 2006, Progress in Materials Science, Vol. 51, pp. 1-60.
- (2) M.Lewandowska, K.J.Kurzydowski. 2005, Materials Characterization, Vol. 55, pp. 395-401.
- (3) J.Eckert, J.C.Holzer, C.E.Krill, III, and W.L.Johnson. 1982, Journal of Materials Research, Vol. 7, pp. 1980-1983.
- (4) C.C.Koch. 1993, Nanostructured Materials, Vol. 2, pp. 109-129.
- (5) J.H.Choi, K.I.Moon, J.K.Kim, Y.M.Oh, J.H.Suh, S.J.Kim. 2001, Journal of Alloys and Compounds, Vol. 315, pp. 178-186.
- (6) F.Zhou, D.Witkin, S.R.Nutt, E.J.Lavernia. 2004, Materials Science and Engineering A, Vol. 375–377, pp. 917–921.
- (7) C.Suryanarayana. 2001, Progress in Materials Science, Vol. 46, pp. 1-184.
- (8) E.J.Lavernia, B.Q.Han, J.M.Schoenung. 2008, Materials Science and Engineering A, Vol. 493, pp. 207–214.
- (9) S.Chatterjee, H.S.Wang, J.R.Yang, K.D.H.Bhadeshia. 2006, Materials Science Technology, Vol. 22, pp. 641-644.
- (10) C.H.Moelle, H.J.Fecht. 1995, Nanostructured Materials, Vol. 6, pp. 421-426.
- (11) A.Tschope, R.Birringer, H.Gleiter. 1992, Journal of Applied Physics, Vol. 71, pp. 5391-5394.

- (12) Z.Lee, D.B.Witkin, V.Radmilovic, E.J.Lavernia, S.R.Nutt. 2005, *Materials Science and Engineering A*, Vol. 410–411, pp. 462–467.
- (13) R.Hayes, V.Tellkamp, E.Lavernia. 1999, *Scripta Materialia*, Vol. 41, pp. 743-748.
- (14) M.Brochu, T.Zimmerly, L.Ajdelsztajn, E.J.Lavernia, G.Kim. 2007, *Materials Science and Engineering A*, Vol. 466, pp. 84–89.
- (15) M.Tokita. Sumitomo Cal Mining Company, Ltd. Internal Communication, p. 13.
- (16) M.Kubota. 2007, *Journal of Alloys and Compounds*, Vols. 434-435, pp. 294-297.
- (17) K.A.Khor, K.H.Cheng, L.G.Yu, F.Boey. 2003, *Materials Science and Engineering A*, Vol. 347, pp. 300-305.
- (18) M. Zadra, F. Casari, A.o Molinari. 2007, *Materials Science Forum*, Vols. 534-536, pp. 1401-1404.
- (19) S.Libardi, M.Zadra, F.Casari, A.Molinari. 2008, *Materials Science and Engineering A*, Vol. 478, pp. 243–250.
- (20) O.Yanagisawa, H.Kuramoto, K.Matsugi, M.Komatsu. 2003, *Materials Science and Engineering A*, Vol. 350, pp. 184-189.
- (21) R.W.Hayes, D.Witkin, F.Zhou, E.J.Lavernia. 2004, *Acta Materialia*, Vol. 52, pp. 4259-4271.
- (22) D.Witkin, Z.Lee, R.Rodriguez, S.Nutt, E.Lavernia. 2003, *Scripta Materialia*, Vol. 49, pp. 297-302.
- (23) R.Rodriguez, R.W.Hayes, P.B.Berbon, E.J.Lavernia. *Acta Materialia*, Vol. 51, pp. 911-929.
- (24) R.W.Hayes, D.Witkin, F.Zhou, E.J.Lavernia. 2004, *Acta Materialia*, Vol. 52, pp. 4259–4271.

- (25) S.Cheng, Y.H.Zhao, Y.T.Zhu, E.Ma. 2007, *Acta Materialia*, Vol. 55, pp. 5822-5832.
- (26) Y.M.Wang, E.Ma. 2004, *Materials and Science and Engineering A*, Vols. 375-377, pp. 46-52.
- (27) R.Kapoor, J.B.Singh, J.K.Chakravartty. 2008, *Materials Science and Engineering A*, Vol. 496, pp. 308-315.
- (28) Y.J.Li, X.H.Zeng, W.Blu. 2004, *Acta Materialia*, Vol. 52, pp. 5009-5018.
- (29) G.J.Fan, H.Choo, P.K.Liaw, E.J.Lavernia. 2006, *Acta Materialia*, Vol. 54, pp. 1759-1766.
- (30) X.Huang, H.Zhang, Y.Han, J.Chen. 2010, *Materials Science Engineering A*, Vol. 527, pp. 485-490.
- (31) E.Evangelista, A.Forcellese, F.Gabrielli, P.Mengucci. *Hot Deformation of Aluminium Alloys*. pp. 121-139.
- (32) Y.V.R.K. Prasad, S.Sasidhara. *Hot Working Guide - A Compendium of Processing Maps*. 1999.

CHAPTER 1

CRYOMILLING AND MICROSTRUCTURAL CHARACTERIZATION OF THE 2024 ALUMINUM ALLOY POWDER

1.1 Mechanical Milling

Mechanical milling is a technique that involves repeated welding and fracturing of the powder particles in a high energy ball mill. Whenever two steel spheres collide and some quantity of powder is trapped between them (see Figure 1), the force of the impact plastically deforms the powder particles leading to work hardening and fracture (1).

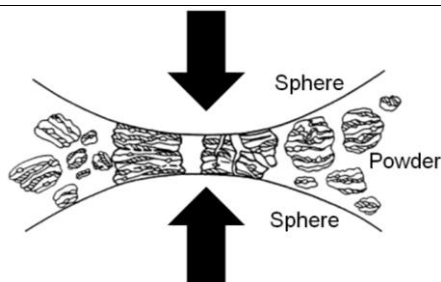


Figure 1: Representation of the ball-to-powder collision during mechanical milling in which two spheres collide and the powder is trapped between them (1).

With continued deformation, the particles get work hardened and fracture by the fragmentation of fragile flakes and/or by a fatigue failure mechanism. Fragments generated by this mechanism can continue decreasing in size in the absence of strong agglomerating forces. At this stage, the tendency to fracture of the particles predominates over cold welding. Due to the continued impact of grinding spheres, the structure of the particles is steadily refined, although the particle remains with same size. Indeed the smaller particles are more resistant to deformation without fracturing and tend to be welded into large parts, with a tendency to drive both very large and very fine particles towards an intermediate size. Consequently, the inter-layer spacing is reduced and the number of layers in a particle is increased. At this stage, particles reach saturation hardness due to the accumulation of strain energy. The particle size distribution at this stage is narrow, because the particles larger than average are actually agglomerates of smaller particles (1). Figure 2 shows the evolution of the particle size during milling.

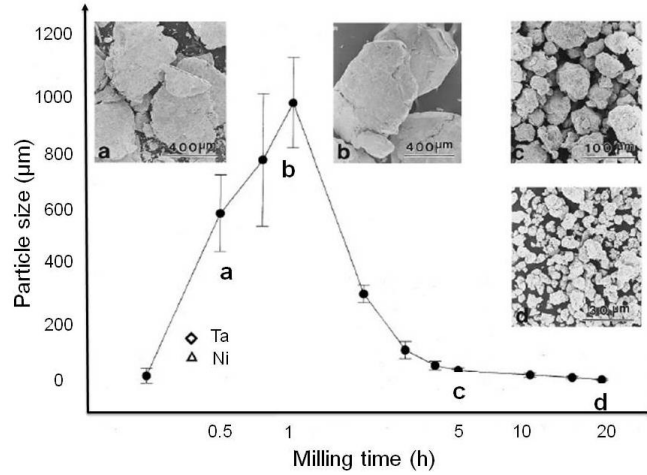


Figure 2: Sharp particle size distribution on milling (1).

Heavy deformation is accumulated by the particles during milling. This is manifested by the presence of the many defects within the crystallites like vacancies, dislocations, stacking faults, and grain boundaries (1).

The achievement of a given structure in any system depends on the parameters used during milling process. It would be a function of the starting particle size as well as of the characteristics of the powder and the milling equipment. However, in the most cases, the rate of refinement of the internal structure (crystallite size, particle size, lamellar spacing, etc.) is roughly logarithmic with processing time and then the starting particles size are not relatively important. In a few minutes to an hour, the crystallite size is refined to nanometric dimensions and the lamellar spacing becomes smaller. Figure 3 shows the refinement of the grain size versus milling time during milling process. The efficiency of the process depends on the ball-to-powder ratio: on increasing this parameter, the energy transferred to the powder increases and the refining is accelerated (1).

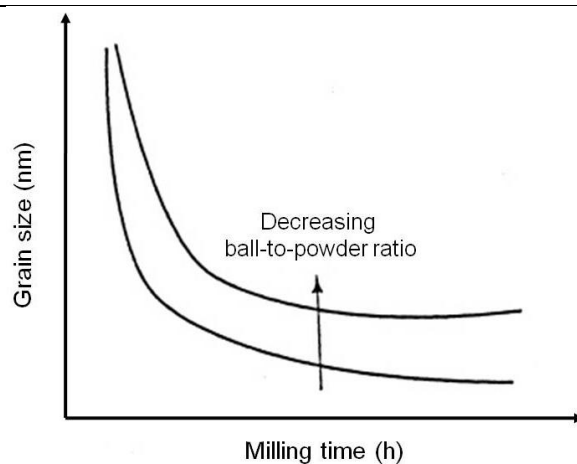


Figure 3: Refinement of crystallite size versus milling time. Rate of refinement enhances on increasing the milling energy and decreasing the ball-to-powder ratio (1).

The main problem of the FCC metals is the necessity to add process control agent (PCA) during milling, as methanol, stearic acid and/or paraffin compounds, to prevent the formation of the agglomerates. Unfortunately, with the addition of the PCA (carbon and oxygen containing) the chemical purity of the material is lost. On the other side, the addition of these agents might be necessary if the objective is increasing the mechanical properties and improve the creep resistance of the material, through the *in-situ* formation of oxides particles (2).

1.1.1 The Formation of the Nanostructure on Milling

Recently, the nanocrystalline materials and the mechanisms responsible for the formation of the nanostructure have been investigated extensively. At the microscopic level, the development of nanostructure during mechanical milling is described in three stages (see Figure 4) (2):

- first stage (I) represents the formation of shear bands with high dislocation density;
- during second stage (II) the annihilation and recombination of dislocations takes place forming small angle sub-boundaries. These sub-grain structures extend in every part of the particle during continued milling;
- final stage (III) characterizes the transformation of sub-grain in randomly oriented high-angle grain boundaries.

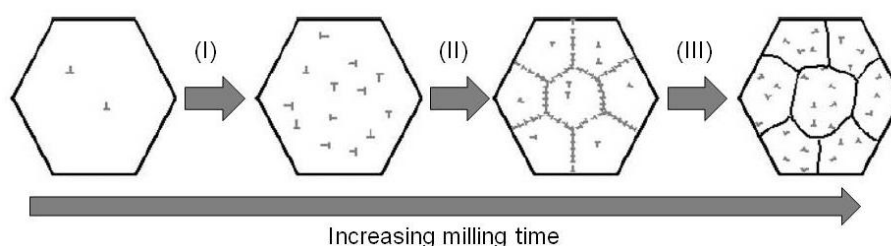


Figure 4: Representation of crystallite refinement mechanism during ball milling process (2).

Plastic deformation caused by milling process can create a very high dislocation density (ρ), that is proportional to stored energy (3). Density of defects increases resulting in increasing of microstrain. It should be noted

that the rate of microstrain accumulation decreases when the grain refinement takes place (see Figure 5). This behaviour indicates that the dislocations tend to rearrange into dipoles minimizing the energy of their strain field. This arrangement of dislocations can be associated with the formation of dislocation walls sub-boundaries resulting in the decrease of the crystallite size (4).

Figure 5 shows the crystallite size and microstrain as a function of milling time of the 2024 Al alloy (5).

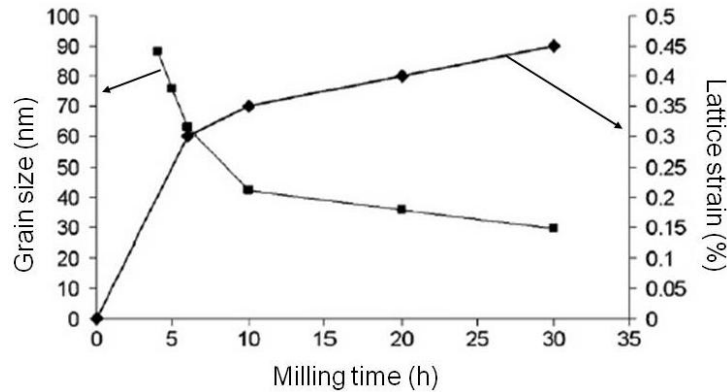


Figure 5: Crystallite size and microstrain of 2024 Al alloy as function of milling time (5).

1.1.2 Minimum Grain Size Obtainable by Milling

The structural refinement through ball milling was studied by (6) with the following conclusions:

- the minimum grain size achievable by milling has scales inversely proportional with the bulk modulus (B) or the melting temperature (T_m);
- grain size decreases on increasing the milling time, obtaining a minimum grain size (d_{min}) that is characteristic of each metal;

- there is a linear relationship between the critical equilibrium distance between two edge dislocations (L_c) and the minimum grain size for FCC nanocrystallite metals;

- limited experiments suggest that smaller nanograin sizes are achieved at lower milling temperatures.

A dislocation model that supports the empirical equation 1 was proposed by Mohamed (6). The minimum grain size is controlled by a balance between the hardening rate introduced by the generation of the dislocation and the recovery rate arising from dislocation annihilation and recombination. The minimum grain size can sustain a dislocation pile-up within grain and it is related to many physical properties of elemental metals (7).

A general empirical relationship for FCC, BCC and HCP systems, including some alloys, can be represented by:

$$\frac{d_{min}}{b} = A \exp[-cT_m] \quad (1)$$

where, A and c are constants, b is the Burgers vector and T_m is the melting temperature.

For FCC metals, a direct relationship between d_{min} and the critical equilibrium distance between two edge dislocations; and an inverse relationship between d_{min} and bulk modulus were proposed (8). Recently, Mohamed et al. (9) demonstrate the relationship between d_{min} and activation energy for recovery, which in turn can be related to melting temperature and bulk modulus.

One consequence is the prediction that milling at lower temperatures will not reduce d_{min} appreciably in metals with lower self-diffusion activation energies, such as Al (2).

Minimum grain size achievable by ball milling for pure Al is around 22 - 25 nm, and it is not expected to further decrease during milling process. This is reasonably due to the high stacking fault energy and low activation energy for dislocation recovery of this metal (6) (7) (8).

Figure 6 shows that despite of the presence of some scatter, data of nanocrystalline metals, regardless to their crystal structure, defines a single curve that is divisible into two parts. In the region where T_m is lower than 2000 K, the normalized minimum grain size (d_{min}/b) decreases rapidly with melting temperature (T_m); it includes the data of the low melting FCC metals (Al, Cu, Ag, Ni, and Pd), Co and Zn (HCP), and Fe (BCC). In the region which T_m is higher than 2000 K, the normalized minimum grain size decreases very slowly with increasing melting temperature; it contains data of the high melting temperature metals: Ir (FCC), Hf and Zr (HCP), and Cr, Nb, and W (BCC) (9).

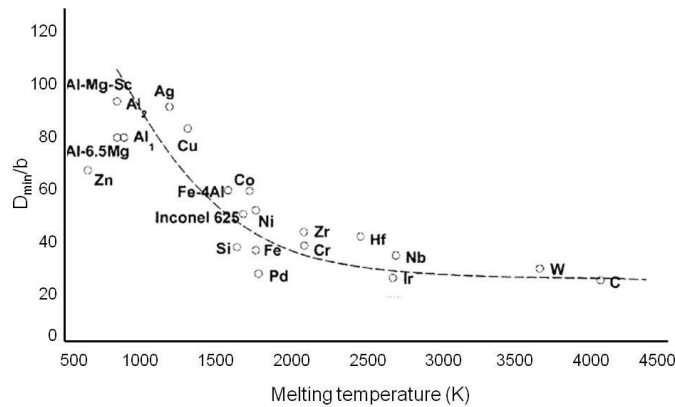


Figure 6: Normalized minimum grain size (d_{min}/b) obtained by milling versus melting temperature (T_m) (9).

1.1.3 Cryogenic Milling

Cryogenic milling is the mechanical attrition where powders are milled in slurry formed by milling steel spheres and liquid nitrogen at low temperature (cryogenic temperature). This is a method of strengthening materials through refinement of the grain size and the dispersion of the fine and nanometric nitrides particles. This technique was developed to decrease the particles size and their spacing within a metallic matrix, increasing the creep resistance and the performance at intermediate temperature (2).

The strength of the material can be enhanced by refining the microstructure regarding to grain size. In this case, possible advantage to using a cryogenic liquid is that the low temperature suppresses the annihilation of dislocations and results in a larger dislocation density (3).

Some advantages of the cryomilling are (10):

- the metal powder may be fractured up to achieves nanostructured grains (less than 100 nm) restricting the formation of the agglomeration and cold welding between particles even without using PCA, resulting in an efficient milling process;
- oxidation reactions are reduced under nitrogen environment protection;
- the milling time required to achieve a nanostructured material is reduced comparing with other processes, because the low temperature suppresses the annihilation of dislocations and the accumulation of a higher dislocation density is favoured (3).

1.2 Experimental Procedures

1.2.1 Cryogenic Milling

Starting powders were produced by Ecka granules by spray atomization. Chemical composition is 4.0% Cu, 1.5% Mg, 0.6% Mn and balance Al.

The 2024 Al alloy powder was processed by cryomilling of a slurry of the powder in liquid nitrogen (-180°C , approximately). The liquid nitrogen was used as lubricant without any PCA. Milling was carried out in a modified Union Process 01-HD attritor (see Figure 7) with a stainless steel vial and balls with 6.0 mm of diameter at a rate of 300 rotations per minute (rpm).

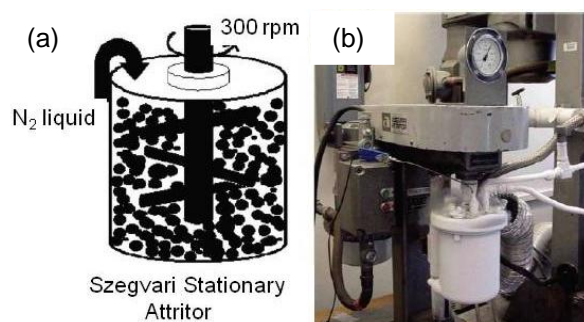


Figure 7: (a) Representation of the Szegvari Stationary Attritor. (b) Attritor machine used to cryomilling.

Ball-to-powder ratios (BPR) were 4:1 (low energy) and 32:1 (high energy) at different times, in order to investigate the influence of the milling energy on the structure and on the thermal stability of the milled powders.

After milling the powders were removed from the attritor and the vial was immediately placed under vacuum to remove any residual liquid nitrogen. Subsequently, powders were stored in argon filled glove-box at room temperature to prevent contamination.

Some milled powders were degassed at 250°C and 350°C for 20h in a Tersid tubular furnace at high vacuum (10^{-5} mbar).

1.2.2 Powder Characterization

Sieve analysis was performed to measure the particle size distribution of as-atomized and as-milled powders. Sieving was carried out separately for each mesh (< 25, 25 - 45, 45 – 90, 90 – 120 and > 120 μm) in agreement with the standard ASTM B214 (11).

In order to obtain the size distribution for finest powders (< 25 μm), the image analysis was performed by Image J® software.

The metallographic investigation was done by Zeiss light optical microscopy (LOM) equipped with a Leica DC300® camera.

Environmental scanning electron microscopy (ESEM) Philips XL 30® (SEM Supra 40 ZEISS, GEMINI column®) was used to observe the particle morphology before and after cryomilling.

Cryomilled powders were analysed by x-ray diffraction (XRD). The diffraction pattern was collected using a Cu $k\alpha$ ($\lambda = 1.5418$) source and an image plate detector over the 2θ range from 10° to 100° in reflection geometry. The experimental spectra were elaborated with the Rietveld method using diffraction MAUD software (12). Line profile analysis was performed with Popa approach to account the possible anisotropy of the crystallite shape (13).

Differential scanning calorimetry (DSC) measurements were performed on Perkin-Elmer DSC7 – TAC7/7 Instrument Controller® under argon at 20 ml/min fluxing atmosphere. Thermal cycles consisted on approximately 15 mg of as-atomized and as-milled powders at different heating rates, from 10 to 40°C/min. Samples were sealed in standard aluminium calorimeter pans. Pure aluminum disks of approximately equal weight was used as reference sample. Measurements started from room temperature to 600°C and the cooling was of 50°C/min. Every sample was processed twice in order to obtain the enthalpy release as the difference between two consecutives scans.

Thermogravimetry (TG) measurements were performed on Netzsch STA 409 PC under argon + H₂ (5%) at 50 ml/min fluxing atmosphere. Thermal cycles consisted on approximately 20 mg of as-milled powder at 20°C/min. The measurements start from room temperature to 550°C and the cooling was of 50°C/min. The zero curve (without powder) was subtracted from the powder curve and the difference between two scans was considered.

Transmission electron microscopy (TEM) observations were performed on the powder using a Philips CM12 microscope operating at 120 kV. Powders were embedded using a G1 resin + hardener and the mixture was poured in copper tube in order to produce thin films. After heating for 10 hours at 60°C to dry the mixture, the sample was sliced in thin disk which were mechanically grounded to a thickness of about 70 µm. After that, ion milled to electron transparency using 6-kV Ar⁺ ions and a thinning angle of 15° was performed. Identification of precipitates was made through selected area electron diffraction patterns (SAEDs) indexing. TEM images were recorded using a dedicated CCD camera.

Heat treatments of milled powders were carried out in a Tersid tubular Furnace in high vacuum (10^{-5} mbar) at different temperatures and times.

1.3 Results and Discussion

Results of the cryogenic milling with BPR 4:1 and BPR 32:1 are presented separately.

Ball-to-powder ratio is a very important variable in the milling process; i.e. the higher the BPR, the shorter is the time to refine the structure. At high BPR, the number of collisions per unit of time increases because of an increase in the weight proportion of the balls. As a consequence, more energy is transferred to the powder particles and then the nanostructure of the material is obtained faster (1).

1.3.1 Cryomilling with BPR 4:1

1.3.1.1 Characterization of the Cryomilled Powder

Figure 8 shows the crystallite size and microstrain as function of milling time.

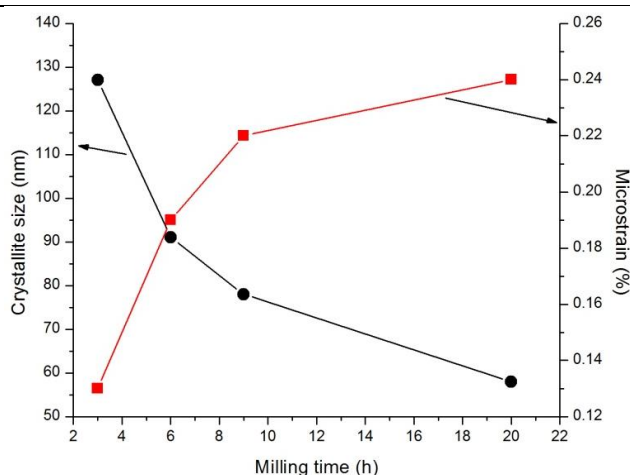


Figure 8: Crystallite size and microstrain of the cryomilled powder at low energy (BPR 4:1) obtained by XRD analyses.

The crystallite size decreases and the internal strain increases on increasing the milling time, as expected (5). After 20h milling, the mean crystallite size is 58 nm and microstrain is 0.24%. Structural characteristics of the milled powder shown in Figure 8 are different from those reported by Jafari et al. (5) which used BPR of 10:1. In particular, the mean crystallite size is larger (58 nm vs. 37 nm) and the microstrain is smaller (0.24% vs. 0.41%). Comparing these results, 20h cryomilled powder using BPR of 4:1 corresponds to 5h cryomilled powder with BPR of 10:1. The efficiency of the milling process reported here is then lower than presented in the literature (5) (14) because of the lower BPR.

Figure 9 shows the particle size distribution and the morphology of the as-atomized and as-milled powders.

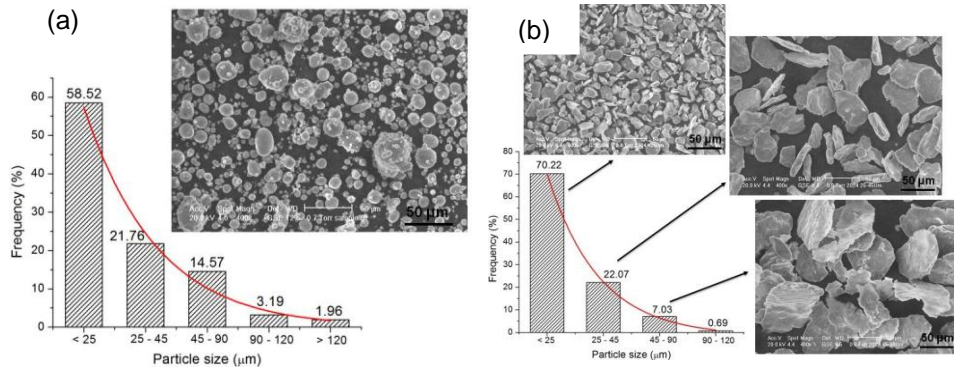


Figure 9: Powder distribution and SEM images of the (a) as-atomized and (b) 20h cryomilled powder at low energy (BPR 4:1).

As-atomized and as-milled powders have particles size sharply distributed. Figure 9a shows well rounded as-atomized particles. Figure 9b shows 20h milled powders that presents relatively coarse and flake-like particles. After milling, the percentage of the finest fraction (< 25 μm) increased from ~ 58% up to ~ 70% at expenses of the other ones, and the fraction > 90 μm decreases from around ~ 5% to ~ 0.7%. The morphology of the as-milled powders indicates that the process did not reach a final stage since milled particles usually have a tendencially rounded morphology. Table 1 reports crystallite size and microstrain of the 20h cryomilled powder obtained by XRD analyses and they are shown separately for three particle size ranges.

Table 1: Crystallite size (D) and microstrain ($\langle \varepsilon^2 \rangle^{1/2}$) of the 20h cryomilled powder at low energy (BPR 4:1).

Particle size (μm)	D (nm)	$\langle \varepsilon^2 \rangle^{1/2}$ (%)
< 25	51	0.26
25 - 45	63	0.21
45 - 90	78	0.17

Crystallites reach nanometric size ($D < 100$ nm); however, even in finest powder the crystallites are quite larger than minimum attainable (6).

1.3.1.2 Thermal Stability of the Cryomilled Powder

It is well known that the thermal stability of the nanostructured materials depends on the balance between the driving force due to the grain boundary surface energy and the resistance force that reduces grain boundary mobility.

Driving force for the grain growth ΔG is the excess of Gibbs free energy correlated to the grain boundary surface, given by equation 2 (15) (16) (17).

$$\Delta G = \gamma \Delta S = \frac{3.3\gamma}{D} \quad (2)$$

where γ is the grain boundary specific energy (from 0.18 to 0.32 J/m² in Al alloys (18)), ΔS is the grain boundary specific surface (m²/m³), D is the mean grain size (m).

Since ΔG increases on decreasing the mean grain size, from a thermodynamic point of view, the smaller the grain size, the larger the tendency to grain growth. Grain boundary mobility is opposed by the presence of geometric dislocations in the adjacent region, which account for the residual strain accumulated on milling (4).

The average microstrain and the grain size determined by XRD (see Table 1) are transformed in a dislocation density as described by (19) in equation 3.

$$\rho = (\rho_D \rho_S)^{1/2} = \frac{2\sqrt{3}\langle \varepsilon^2 \rangle^{1/2}}{Db} \quad (3)$$

where ρ is the dislocation density (m^{-2}), ρ_D is dislocation density due to the grain size (m^{-2}), ρ_S is dislocation density due to the microstrain (m^{-2}), D is the grain size (m), $\langle \varepsilon^2 \rangle^{1/2}$ is the root-mean-square lattice microstrain (%) and b is the modulus of Burgers vector (assumed 0.286×10^{-9} m).

Dislocation densities for three particle size ranges are reported in Table 2.

Table 2: Dislocation densities of the 20h milled powder at low energy (BPR 4:1) calculated by equation 3.

Particle size (μm)	D (nm)	ρ (m^{-2})
< 25	51	0.68×10^{15}
25-45	63	0.44×10^{15}
45-90	78	0.29×10^{15}

Since the grain boundary is described as an array of dislocation, the resistance offered by strain accumulated between and within the crystallite

can be expressed by the stress required to move dislocation against (20). From micromechanics point of view, it can be assumed that the grain boundary motion is driven by the stress τ_1 resulting from the driving force of grain growth and it is opposed by the resistance τ_2 , the drag force induced by the dislocations in the strained regions. Grain growth can occur if τ_1 is higher than τ_2 (21). Figure 10 is a representation of the two main stresses acting on the grain boundary.

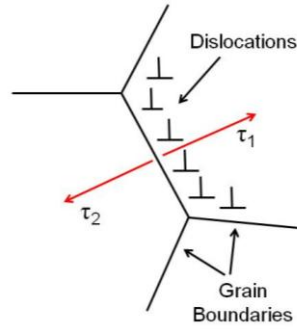


Figure 10: Representation of the driving stress τ_1 and resistance stress τ_2 on the grain boundary surface.

Driving stress (τ_1) is expressed by equation 4 (20).

$$\tau_1 = \phi \Delta G = \phi \gamma \Delta S = \frac{3.3 \phi \gamma}{D} \quad (4)$$

where ϕ is a constant assumed equal to unity, ΔG is magnitude of the driving force, ΔS is grain boundary specific surface, D is mean crystallite size (m), and γ is specific energy of the grain boundary (J/m^2).

Resistance stress (τ_2) is given by equation 5 (20).

$$\tau_2 = \frac{Gb\rho^{\frac{1}{2}}}{8\pi(1-\nu)} \quad (5)$$

where G is shear modulus (assumed 0.262×10^{11} Pa), b is modulus of the Burgers vector (assumed 0.286×10^{-9} m), ρ is dislocations density and ν is Poisson's ratio (assumed 0.345).

Driving and resisting stresses are listed in Table 3. The driving stress is calculated using 0.25 J/m^2 , an average value of the grain boundary specific energy (18).

Table 3: Calculus of the driving (τ_1) and resistance (τ_2) stresses on the grain boundary for 20h cryomilled powder at low energy (BPR 4:1).

Particle size (μm)	D (nm)	τ_1 (N/mm^2)	τ_2 (N/mm^2)	$\tau_1 - \tau_2$ (N/mm^2)
< 25	51	1.64×10^7	1.19×10^7	0.45×10^7
25-45	63	1.33×10^7	0.95×10^7	0.38×10^7
45-90	78	1.07×10^7	0.77×10^7	0.30×10^7

Stresses decrease on increasing the crystallite size; however τ_1 is always higher than τ_2 . It is evident that the resistance stress is lower than the driving one, and then thermal stability of the nanostructured powders should be rather low. As a consequence, a rapid increase of grain size is expected during heating.

1.3.1.3 Incoherent Precipitation on Ageing of the Cryomilled Powder

The influence of the nanostructure on the transformations on ageing of the Al alloy was investigated by XRD. Given the difficulty of detecting coherent precipitates by means of conventional XRD technique, the attention was found on the incoherent precipitates. The phase transformations on heating of three granulometric fractions of the 20h milled powder were investigated at temperatures from 475°C to 525°C, where incoherent precipitation occurs (22).

According to Badini et al. (23), two different ageing sequences can occur separate or contemporaneously depending on the Cu content and the Cu:Mg ratio in the alloy. During artificial ageing of these as-quenched alloys Al-Cu and/or Al-Cu-Mg metastable phases take place. If the ageing treatment is carried out for a long time, the stable incoherent Al_2Cu (θ) and/or Al_2CuMg (S) phases occur according to the isothermal section at the ageing temperature of the Al-Cu-Mg phase diagram.

The decomposition of supersaturated Al-Cu solid solution results in the formation of the phases: GP zone $\rightarrow \theta'' \rightarrow \theta' \rightarrow \theta$ (Al_2Cu). The formation of a supersaturated Al-Cu-Mg solid solution leads to the following precipitation sequences: GPB zone $\rightarrow \text{S}' \rightarrow \text{S}$ (Al_2CuMg) (23) (24) (25).

According to Jena et al. (26), the semi-coherent precipitate is only slightly strained version of incoherent precipitate and with increase in temperature semi-coherent gradually relaxes to become the strain free incoherent phase. It means that the material requires a reorganization of the precipitate structure to reduce the lattice strain.

The strain associated with a nucleus will enlarge as its size increases, although its size cannot increase indefinitely. It is possible that the particle can break away from the lattice of the matrix, and when this occurs, a surface, or grain boundary, forms between two planes. Such a loss of coherency would greatly reduce the state of strain associated with the precipitate particles. It means that the strains associated with the coherency are lost or reduced when a new phase that is non-coherent or less coherent forms. With the growing particle size, the total nonchemical energy of the particle (strain + surface energy) may be reduced if a coherent boundary is replaced by a semi-coherent boundary (27).

XRD analyses of the as-milled powders do not reveal any peaks of intermetallic compounds, suggesting that the as-milled alloy is in solution annealed condition. This finds a confirmation in literature (5), which reports solution annealing induced by mechanical alloying in a 4% Cu and 1.9% Mg alloy.

Two incoherent precipitates (θ and S) were detected. The thermodynamic equilibrium predicts the existence of the two precipitates at 350°C, and only of θ at 550°C after 3 hours of annealing (5). On the other side, Badini et al. (23) report the presence of the ternary S phase at 500°C, as well.

The effect of temperature and time on the amount of these precipitates is reported in Figure 11, Figure 12 and Figure 13, relevant to the < 25, 25 - 45 and 45 - 90 μm milled powders, respectively.

In the finest powder (see Figure 11), S decreases with time, whilst θ increases at the lower temperature, decreases at the higher, and have an intermediate trend at 500°C. On increasing temperature, S decreases and disappears at 500°C after 10 minutes and even for the shortest time at 525°C.

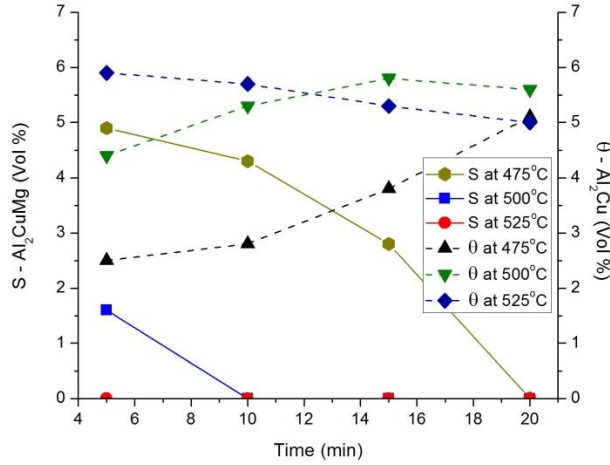


Figure 11: XRD analyses of the Al₂CuMg and Al₂Cu precipitates of granulometric class < 25 μm.

In the intermediate powder (see Figure 12), again θ increases and S decreases with holding time. On increasing temperature, S decreases and θ increases.

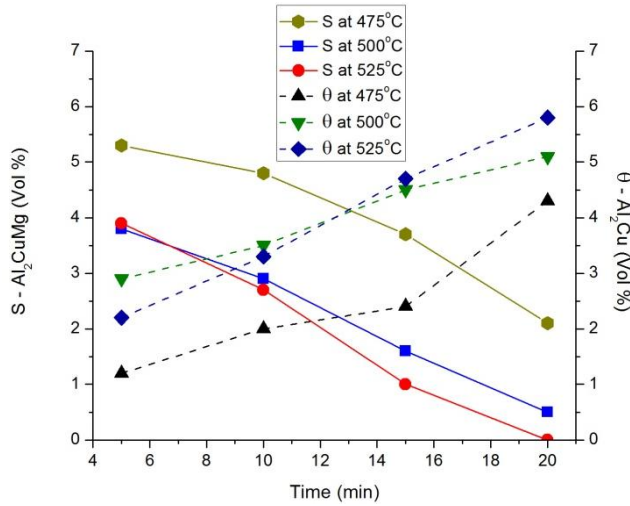


Figure 12: XRD analyses of the Al₂CuMg and Al₂Cu precipitates of granulometric class 25 - 45 μm.

In the coarser powder (see Figure 13), θ increases and S decreases with the isothermal holding time. The increase the temperature, decreases the amount of S and, from 475°C to 525°C, increases the amount of θ .

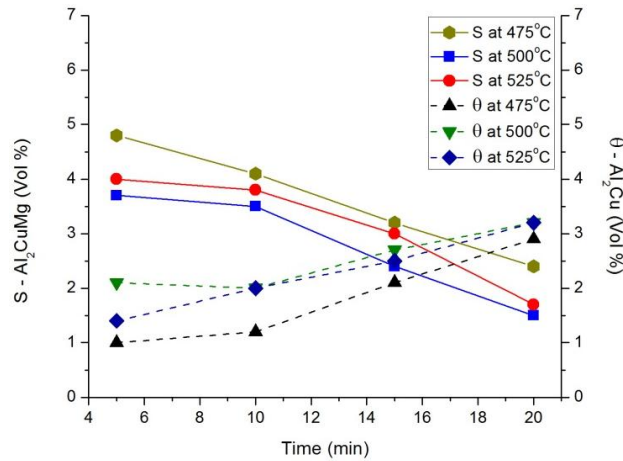


Figure 13: XRD analyses of the Al₂CuMg and Al₂Cu precipitates of granulometric class 45-90 μm.

In general, the trend depicts a transition from S to θ on increasing temperature and time, enhanced by the decrease of the particle size, i.e. by the decrease of the crystallite size and/or the increase in the lattice strain. The effect is particularly evident in the finest powder, which does not contain any S at 525°C and, after 10 minutes, at 500°C. At the highest temperature, even θ tends to decrease in amount.

According to Jafari et al. (5), the Mg atoms have greater influence on Al lattice parameter than Cu, due to Mg atom to be bigger compared to Cu atom. Simultaneously, Al lattice parameter increases as a result of presence of Mg in Al lattice. The lack of S phase and formation of θ phase in this case can be attributed to the lower diffusivity of bigger atoms Mg compared to Cu atoms.

Furthermore, the volume of the lattice structure of θ phase is 0.1798 nm^3 and it has body-centred tetragonal structure with lattice spacing of $a = 0.607$ and $c = 0.488 \text{ nm}$. The volume of S precipitate is 0.2636 nm^3 and it presents orthorhombic structure with the lattice parameters of $a = 0.400$, $b = 0.923$ and $c = 0.714 \text{ nm}$ (28).

With respect to the transition between S and θ , the transformation arises early in finest structure, because it tends to achieve the equilibrium more quickly due the accumulated energy.

1.3.2 Cryomilling with BPR 32:1

1.3.2.1 Characterization of the Cryomilled Powder

Figure 14 shows the crystallite size and microstrain versus milling time.

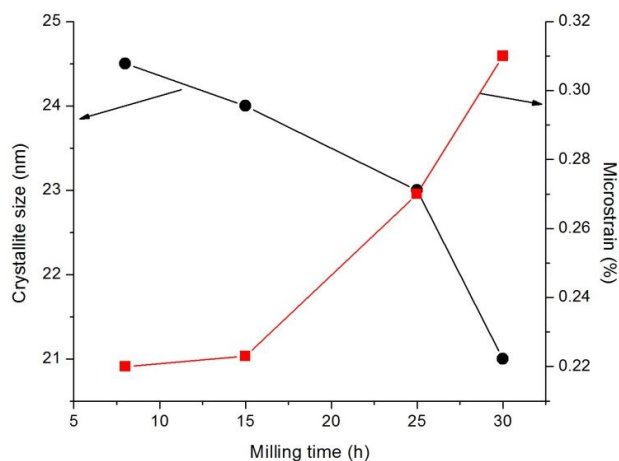


Figure 14: Crystallite size and microstrain of the cryomilled powder at high energy (BPR 32:1) obtained by XRD analyses.

After 30h milling at high energy, the grain size is 21 nm and the lattice strain is 0.31. The crystallite size obtained at high energy is significantly smaller than that obtained with BPR of 4:1, as expected. The lattice strain is larger, accordingly.

Figure 15 shows the particle size distribution and the morphology of the 8h and 25h milled powders.

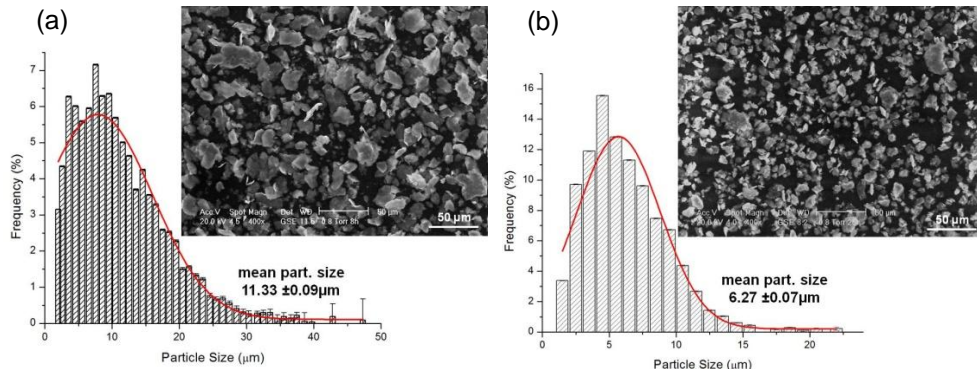


Figure 15: Powders distribution and SEM images of the (a) 8h and (b) 25h cryomilled powder at high energy (BPR 32:1).

Particles are flake-like and present a sharp distribution. The most part of the particles is below 30 μm for 8h and below 15 μm for 25h. The mean particle size is 11.3 μm and 6.3 μm for 8h and 25h powders, respectively.

Figure 16 shows TEM images of the 8h cryomilled powder. Bright field (BF), dark field (DF) and select area electron diffraction (SAED) are shown.

Figure 16 shows nanometric grains which measuring around 20 - 100 nm.

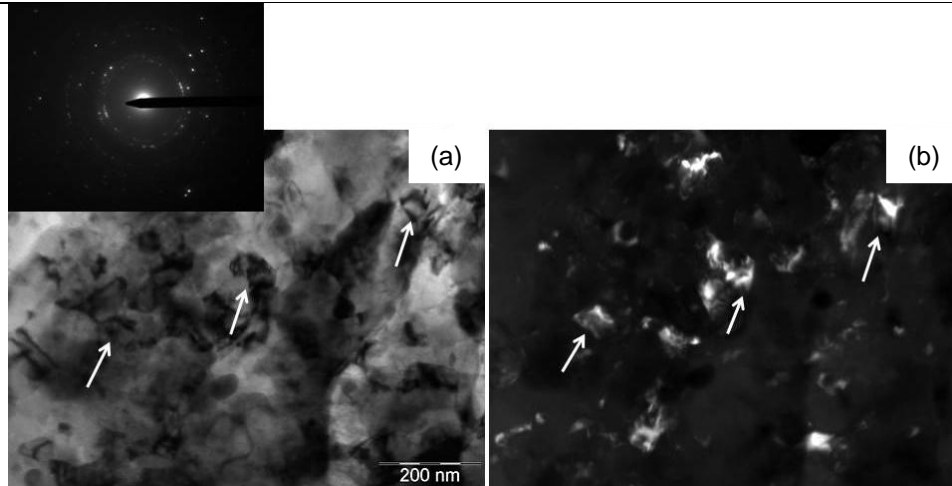


Figure 16: (a) SAED pattern, bright field (BF) and (b) dark field (DF) are shown in TEM micrographs of the 8h milled powder at high energy (BPR 32:1). The nanograins are evidenced by the arrows.

1.3.2.2 Thermal Stability of the Cryomilled Powder

Table 4 reports dislocation densities calculated by XRD for as-milled powders.

Table 4: Dislocation densities of the cryomilled powders at high energy (BPR 32:1) calculated by XRD.

Milling time (h)	Particle size (μm)	D (nm)	ρ (m^{-2})
8	< 30	24.5	1.15×10^{15}
25	< 15	23	1.80×10^{15}

Driving and resistance stresses were calculated and listed in Table 5. The grain boundary specific energy used was 0.25 J/m^2 (18).

Table 5: Driving (τ_1) and drag stresses (τ_2) on the grain boundary of the 8h and 25h cryomilled powders at high energy (BPR 32:1).

Milling time (h)	Particle size (μm)	D (nm)	τ_1 (N/mm^2)	τ_2 (N/mm^2)	$\tau_1 - \tau_2$ (N/mm^2)
8	< 30	24.5	3.41×10^7	1.54×10^7	1.87×10^7
25	< 15	23	3.63×10^7	1.93×10^7	1.70×10^7

The drag stress is lower than the driving one. As a consequence, nanostructured powder milled at high energy has low thermal stability. Meanwhile, ball-to-powder ratio of 32:1 is effective to nanostructure 2024 Al alloy powder. The grain size of the powder cryomilled for 25h is too fine for safe handling and processing. On the other hand, 8h cryomilled powder has grain size values close to d_{min} and the particles are not extremely fine. Values for grain size, microstrain and dislocation density present a slight difference between 8 and 25h cryomilled powders. Therefore, further experiments were carried out on the 8h milled powder.

1.3.2.3 Transformations on Heating of the Cryomilled Powder

Figure 17 shows DSC curves at four different heating rates for as-atomized and 8h milled powders. Similar peaks are observed in DSC traces for both powders.

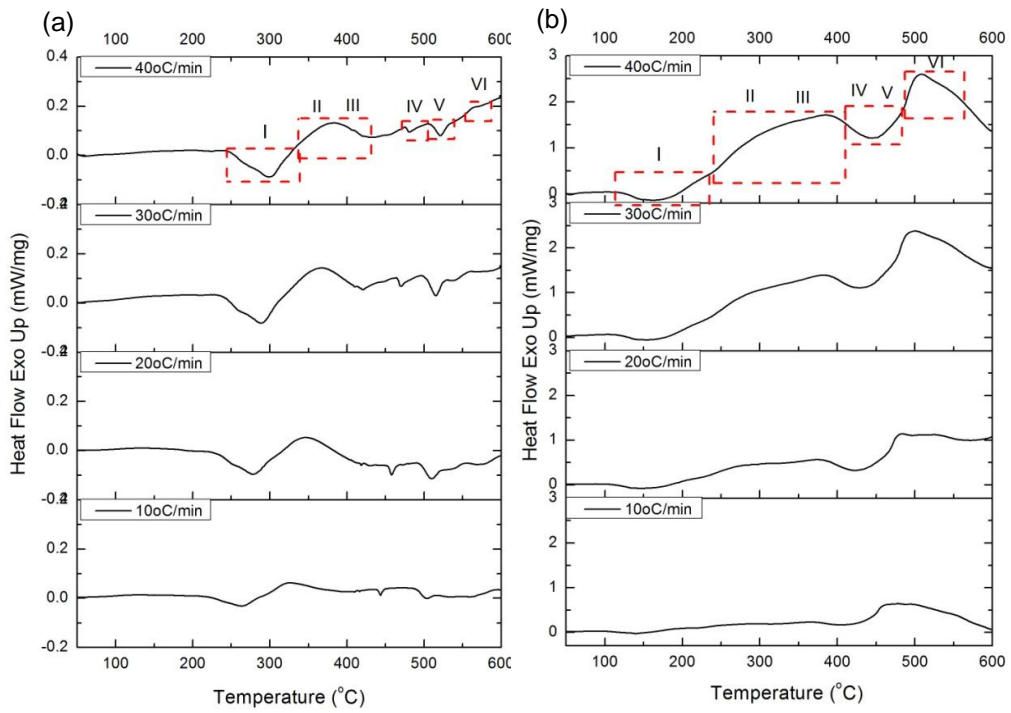


Figure 17: DSC curves of the (a) as-atomized and (b) 8h cryomilled powders at high energy (BPR 32:1) using heating rate of 10, 20, 30 and 40 °C/min.

DSC curves of powders present an endothermic peak (I) at around 250 - 330°C for as-atomized and at 110 - 240°C for as-milled powders. It represents the dissolution of GP zones formed during heating (23) (22).

The precipitation of GP zones is already present in both powders.

According to Wang et al. (29), the subsequent large exothermic peak (II and III) at 330 - 420°C for as-atomized and at 250 - 420°C for as-milled powders is attributed to precipitation of coherent θ'' and semi-coherent θ'/S' phases.

Endothermic peaks (IV and V) at 470 - 500°C and 500 - 540°C for as-atomized and at 420 - 490°C for as-milled have different shapes. The as-atomized powder presents two endothermic peaks and the as-milled displays just an endothermic peak, in which both peaks are probably overlapped. These peaks define the dissolution of θ'' and θ'/S' phases (30).

The last exothermic peak (VI) at 550 - 570°C for as-atomized and at 490 - 550°C for as-milled powders represent the precipitation of incoherent θ/S phase and it can be related to structural relaxation and/or grain growth (22) (31).

DSC curves of the as-milled powder present a broad exothermic effect over the whole temperature range investigated. It should be attributed to strain recovery and grain growth of the powder on heating.

An anticipation of transformations involving GP zones and precipitates is reported by Badini et al. (23) in a SiC reinforced Al alloy. This effect is attributed to the strain accumulated at the interface between the reinforce particle and the metallic matrix. The same effect can be here claimed to justify the shift of the nanostructured powder peaks, since the milled powder contains a large lattice strain due to the nanostructure obtained on

milling process. The milling introduces a high dislocation density into the material, which provides large quantities of preferential nucleation sites for precipitation and accelerates the precipitation, because it reduces the energy barrier of nucleation and the activation energy for precipitates formation. DSC traces show that the addition of the defects inside the material through milling process no changes the precipitation sequence on heating; however it increases the kinetics (29).

1.3.2.4 Degassing of the Cryomilled Powder

Thermogravimetric analyses were carried out in order to study the degassing process on the powders.

Figure 18 shows 8h milled powder on heating with a weight loss of 12.33% which starts at the beginning of TG analysis up to 500°C.

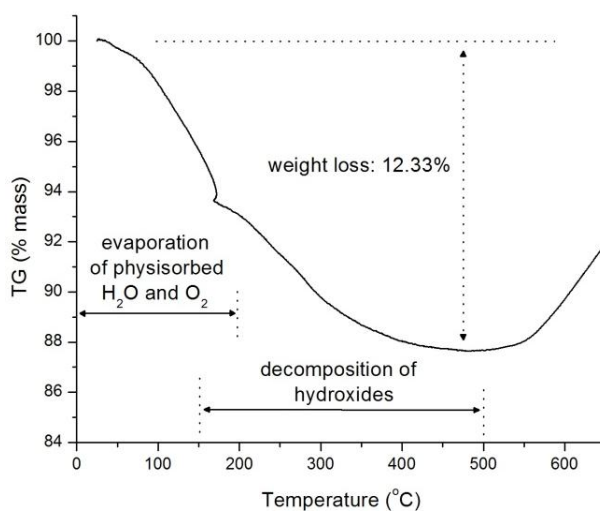


Figure 18: Thermogravimetric analysis of the 8h cryomilled powder upon heating rate of 20°C/min.

It is well known that the surface of the Al powders, when in contact with the air, is always covered with a thin aluminium oxide layer (Al_2O_3) which is hydrated because of the air humidity. On heating, the physisorbed water and oxygen evaporate first, after that the decomposition of the hydroxides on the surfaces occurs. Besides oxidation, surface particles can have adsorbed nitrogen from milling slurry, that is also eliminated on heating (32). These reactions lead to a weight loss, as shown the Figure 18.

Figure 19 shows the thermogravimetric analyses of the 8h cryomilled powders degassed at 350 and 250°C for 20h.

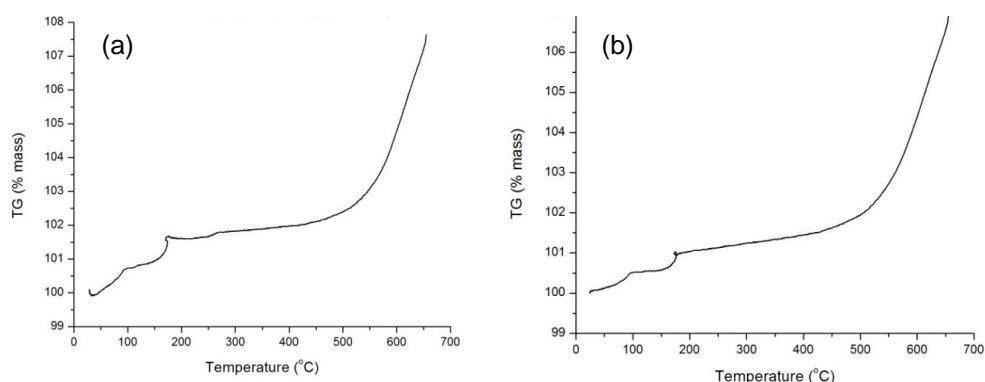


Figure 19: Thermogravimetric analyses of the 8h cryomilled powder degassed at (a) 250°C and (b) 350°C for 20h upon heating rate 20°C/min.

After degassing, the powders do not display weight loss, since the gases on the surface particles have been eliminated during degassing.

When the temperature rises, the dislocation density diminishes and crystallites start growing. XRD analysis shows that the mean size of crystallites is larger than 100 nm after degassing. As a consequence, the nanostructure of the 8h cryomilled powder at high energy (BPR 32:1) is partially lost after degassing.

1.3.2.5 Transformation on Heating of Cryomilled and Degassed Powder

Figure 20 shows DSC curves of the 8h cryomilled powder degassed at 250 and 350°C for 20h.

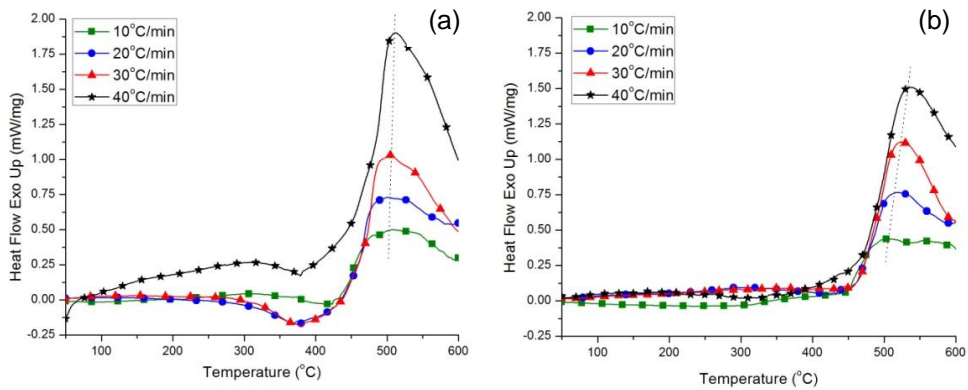


Figure 20: DSC curves of the 8h cryomilled powder at high energy (BPR 32:1) degassed at (a) 250°C and (b) 350°C for 20h.

All phase transformations have already occurred during degassing, except the incoherent precipitation that is represented by sharp exothermic peak. Besides exothermic peak, the degassed powder at 250°C presents traces of the endothermic reaction from 300 up to 420°C approximately. It should correspond to nucleation, growth and/or coarsening of the coherent and semi-coherent precipitates (33) (34).

The position of the peaks shifts to higher temperature and their intensities become higher when the heating rate increases (32). These phenomena are expected from the thermal analysis theory (35).

Activation energy of the exothermic peak is calculated based on the peak position (T) in DSC curves as a function of heating rate (β) according to Ozawa method (36):

$$\ln\left(\frac{1}{\beta}\right) = \frac{Q}{RT} + C \quad (6)$$

where, C is a constant, Q is the activation energy of the process (J/mol), R is the perfect gas constant (assumed 8.314 J/mol.K) and T is the specific absolute temperature (K) corresponding to the peak temperature of the process.

Figure 21 shows the plot of Ozawa's equation of the analyses carried out on two DSC experiments.

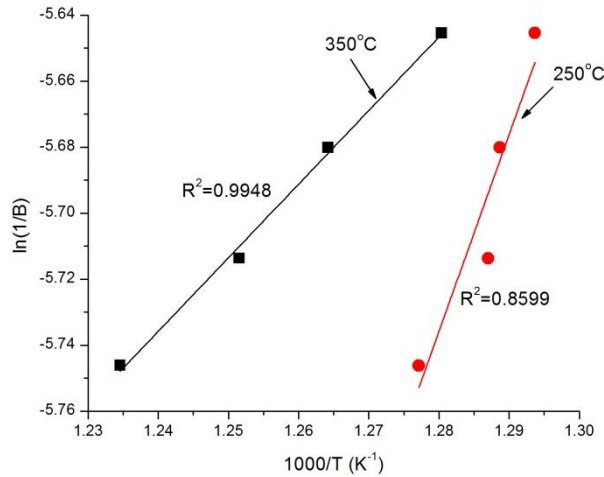


Figure 21: Activation energy (Q) plot for exothermic peaks observed of the 8h cryomilled powder and degassed at 250 and 350°C.

Table 6 shows the activation energy calculated for 8h cryomilled and degassed powders.

Table 6: Activation energy calculated by Ozawa method from DSC scans with different heating rates (10, 20, 30 and 40°C/min) for 8h cryomilled powders and degassed at 250 and 350°C.

Q (KJ/mol)	
250°C 20h	350°C 20h
49.58 ±11.25	18.53 ±0.77

Activation energy values are quite low and there is no correlation to literature data on coherent precipitation and grain growth. They can then represent the transformation from coherent to incoherent precipitation.

1.4 Summary

A nanostructured 2024 Al alloy powder is obtained using cryogenic milling in liquid nitrogen. The powder is cryomilled with ball-to-powder ratio 4:1 and 32:1. There is a direct correlation between particle size and crystallite size, with the increase in lattice defects obtained through the fragmentation of the powder during cryogenic milling.

Increasing the BPR and the milling time, particles become finer. After milling at low and high energy, the particle morphology indicates that the process did not reach a final stage since usually milled particles have a fine and tendentially rounded morphology.

The crystallite size of the 20h cryomilled powder with BPR of 4:1 is coarse and quite higher than minimum grain size. On the other hand, the grain size of the powder cryomilled for 25h with BPR of 32:1 is close to d_{min} , however particles are too fine for safe handling and processing. Consequently, the 8h cryomilled powder with BPR of 32:1 presents grain size values close to d_{min} and not extremely fine particle size. So it was selected for next experiments.

DSC analyses show the precipitation and the dissolution of the GP zones, θ'' , θ'/S' and θ/S for as-atomized and cryomilled powder at high energy (BPR 32:1). Similar peaks are observed in the DSC traces in both powders, but nanostructure activates all the transformations.

Thermal stability is supposed to be low. The resistance stress to grain growth due to microstrain is much lower than the driving one. This

suggests that the grain size increases rapidly on heating 8h cryomilled powder.

Oxygen and nitrogen can be eliminated by degassing for 20h at 250 and 350°C. However, degassing treatment promotes grain growth and the degassed powder presents a larger structure ($D > 100$ nm).

REFERENCES

- (1) C.Suryanarayana. 2001, Progress in Materials Science, Vol. 56, pp. 1-184.
- (2) D.B.Witkin, E.J.Lavernia. 2006, Progress in Materials Science, Vol. 51, pp. 1-60.
- (3) F.Zhou, X.Z.Liao, Y.T.Zhu, S.Dallek, E.J.Lavernia. 2003, Acta Materialia, Vol. 51, pp. 2777–2791.
- (4) I.Lonardelli. *PhD Thesis*. April 2010. pp. 1-111.
- (5) M.Jafari, M.H.Enayati, M.H.Abbasi, F.Karimzadeh. 2009, Journal of Alloys and Compounds, Vol. 478, pp. 260-264.
- (6) F.A.Mohamed. 2003, Acta Materialia, Vol. 51, pp. 4107-4119.
- (7) F.Zhou, D.Witkin, S.R.Nutt, E.J.Lavernia. 2004, Materials Science and Engineering A, Vol. 375–377, pp. 917–921.
- (8) J.Eckert, J. C.Holzer, C.E.Krill, W.L.Johnson. 1982, Journal of Materials Research, Vol. 7, pp. 1980-1983.
- (9) F.A.Mohamed, Y.Xun. 2003, Materials Science and Engineering, Vol. A354, pp. 133-139.
- (10) E.J.Lavernia, B.Q.Han, J.M.Schoenung. 2008, Materials Science and Engineering A, Vol. 493, pp. 207–214.
- (11) ASTM B214-07. Standard Test Method for Sieve Analysis of Metal Powders.
- (12) L.Lutterotti, S.Matthies, H.R.Wenk, A.S.Shultz, J.W.Richardson. 1997, Journal of Applied Physics, Vol. 81, pp. 594-600.

- (13) N.C.Popa. *Journal of Applied Crystallography*. 1998. Vol. 31, pp. 176-180.
- (14) Z.Lee, D.B.Witkin, V.Radmilovic, E.J.Lavernia, S.R.Nutt. 2005, *Materials Science and Engineering A*, Vol. 410–411, pp. 462–467.
- (15) C.H.Moelle, H.J.Fecht. 1995, *Nanostructured Materials*, Vol. 6, pp. 421-426.
- (16) A.Tschope, R.Birringer, H.Gleiter. 1992, *Journal of Applied Physics*, Vol. 71, pp. 5391-5394.
- (17) L.C.Chen, F.Spaepen. 1991, *Journal of Applied Physics*, Vol. 69, pp. 679-688.
- (18) H.Zhang, M.Upmanyu, D.J.Srolovitz. 2005, *Acta Materialia*, Vol. 53, pp. 79-86.
- (19) Y.H.Zhao, K.Lu, K.Zhang. 2002, *Physical Review B*, Vol. 66, 085404.
- (20) S.Chatterjee, H.S.Wang, J.R.Yang, K.D.H.Bhadeshia. 2006, *Materials Science and Technology*, Vol. 22, pp. 641-644.
- (21) A.Molinari, I.Lonardelli, K.Demetrio, C.Menapace. 2010, *Journal of Materials Science*, Vol. 45, pp. 6739–6746.
- (22) M.Murayama, Z.Horita, K.Hono. 2001, *Acta Materialia*, Vol. 49, pp. 21-29.
- (23) C.Badini, F.Marino, E.Verne. 1995, *Materials Science and Engineering A*, Vol. 191, pp. 185-191.
- (24) C.C.Koch. 1993, *Nanostructured Materials*, Vol. 2, pp. 109-129.
- (25) G.E.Totten, D.S.Mackenzie. *Handbook of Aluminum*. s.l: Basel. Vol. 1.
- (26) A.K.Jena, A.K.Gupta, M.C.Chaturvedi. 1989, *Acta Materialia*, Vol. 37, pp. 885-895.
- (27) R.E.Reed-Hill. *Physical Metallurgy Principles*. 3rd. 1992.

- (28) M.Gao, C.R.Feng, R.P.Wei. 1998, *Metallurgical and Materials Transactions A*, Vol. 29, pp. 1146-1151.
- (29) X.Wang, G.Wu, D.Sun, L.Jiang, Y.Han. 2004, *Material Science and Technology*, Vol. 20, pp. 167-172.
- (30) M.Khitouni, R.Daly, A.W.Kolsi, N.Njah. 2006, *Physical Status Solidi*, Vol. 3, pp. 3341-3346.
- (31) F.Zhou, J.Lee, S.Dallek, E.J.Lavernia. 2001, *Journal of Material Research*, Vol. 16, pp. 3451-3458.
- (32) L.Shaw, H.Luo, J.Villegas, D.Miracle. 2003, *Acta Materialia*, Vol. 51, pp. 2647-2663.
- (33) I.N.Khan, M.J.Starink, J.L.Yan. 2008, *Materials Science and Engineering A*, Vol. 472, pp. 66-74.
- (34) T.S.Kim, T.H.Kim, K.H.Oh, H.I.Lee. 1992, *Journal of Materials Science*, Vol. 27, pp. 2599-2605.
- (35) R.F.Speyer. *Thermal Analysis of Materials*. New York: Marcel Dekker, 1994.
- (36) G. Benchabanea, Z. G.Benchabane, Z.Boumerzoug, I.Thibon, T.Gloriant. 2008, *Materials Characterization*, Vol. 59, pp. 1425-1428.

CHAPTER 2

SINTERING OF THE BIMODAL ULTRA-FINE GRAINED/MICROMETRIC POWDERS BY SPARK PLASMA SINTERING

2.1 Spark Plasma Sintering

The Spark Plasma Sintering (SPS), also called pulsed electric current sintering (PECS), is a relatively new technology that can consolidate powders at lower temperature and in a shorter time than other methods (1).

Figure 1 represents the schematic system configuration of the SPS. Graphite die and punch set are filled with the powder.

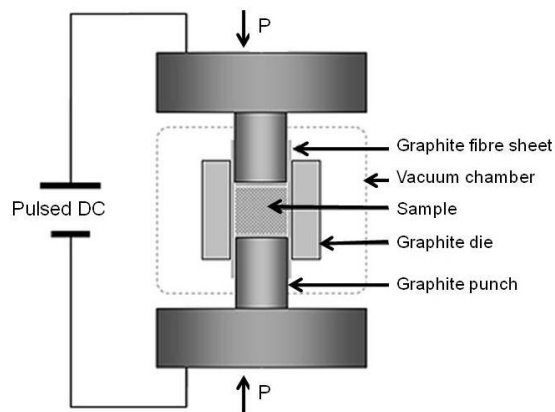


Figure 1: Sintering chamber where the powder is placed in a graphite die during SPS process.

SPS is similar to hot pressing which a uniaxial pressure is applied to the powder during sintering process. However, SPS process has many advantages over alternative sintering methods. First of all, the materials can be sintered in a few minutes, as opposed to hours. Also, temperatures needed to consolidate samples to reach full density are lower. This opens up the possibility of creating materials with nano-scale structural features. SPS is capable of sintering traditionally difficult-to-sinter materials, such as tungsten carbide and titanium alloys, with relative ease and without the benefit of sintering aids (2).

In SPS process, a pulsed direct current (DC) is applied and electrical discharges activate the powder particles. A uniform sintering occurs because when the neck between the particles has been formed, the electric resistivity momentarily falls down and a high current flow takes place. Temperature increases and also the electric resistivity; consequently the current flow diverges to other points, and welds between other particles form (2) (3).

Four factors contribute to the fast densification process (4):

- an efficient heat transfer;
- the use of high pressure;
- the presence of the electrical field (use pulsed direct current fields);
- the presence of local spark discharges generated between the particles under high energy electrical pulses.

Figure 2 represents the pulsed current that flows through the conductive powder particles.

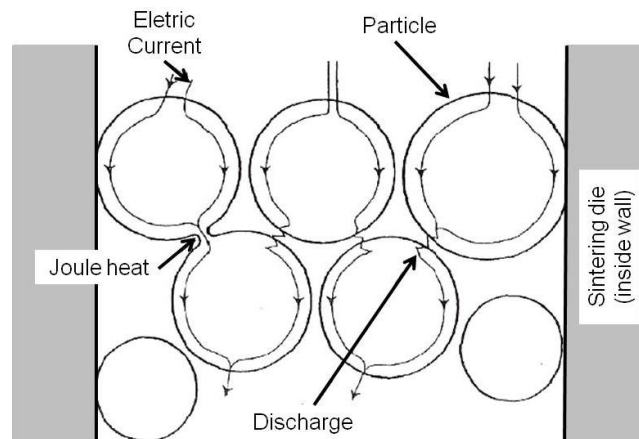


Figure 2: Pulsed current flow through conductive powder particles (5).

For non-conductive powders, heating occurs through heat transfer from die and punches. With the application of alternating DC current, thermal and electrical breakdown phenomena are most likely to occur at high temperatures, and the current can flow through the non-conductive ceramic powder (2).

It is well known that aluminium powders are hardly sinterable materials because of the oxide layer on their surface. The rapid heating and the discharge at contact points causes fragmentation of the oxide layers. This

layer is break and the neck formation and growth is activated. The pressure is applied promoting mass transport by plastic flow and creep (6).

2.2 Experimental Procedures

2.2.1 Spark Plasma Sintering

Spark Plasma Sintering (SPS) was carried out on a DR. SINTER® SPS1050 (Sumitomo Coal & Mining, now SPS Syntex Inc.) apparatus with graphite punches and die.

Cylindrical samples were sintered at a range of 350 - 525°C, pressure of 60 MPa, holding time of 1 minute and free cooling. Temperature was measured by K-thermocouple inserted into the die and a nominal temperature was obtained (it is not the real temperature of the sample).

2.2.2 Characterization of the Sintered Samples

Determination of the density was performed by Archimedes method, according to standard ASTM B 962 (7). The Archimedes density (ρ_s) was calculated by equation 1.

$$\rho_s = \left(\frac{m}{m - m_a} \right) \rho_{water} \quad (1)$$

where m is the mass of the sample, m_a is the apparent mass and ρ_{water} is the density of water.

Measurements were carried out with a precision balance Adventurer Pro AS214 OHAUS® with sensibility of 0.0001g.

The metallographic characterization was carried out by a Zeiss light optical microscopy (LOM) equipped with a Leica DC300® camera microscopy. Sintered samples were prepared through the classical metallurgical preparation and their surfaces were etched by Keller's reagent (190 ml of distilled water, 3 ml of hydrochloric acid, 5 ml of nitric acid and 2ml of hydrofluoric acid).

Environmental scanning electron microscopy (ESEM) Philips XL 30® (SEM Supra 40 ZEISS, GEMINI column®) was used to characterize the microstructure of the samples.

Transmission electron microscopy (TEM) observations were performed on the sintered samples using a Philips CM12 microscope operating at 120 kV. Samples were mechanically grounded to a thickness of about 70 µm and then ion milled to electron transparency using 6-kV Ar⁺ ions and a thinning angle of 15° was performed. Identification of precipitates was made through several nanoprobe analyses (EDXS), together with selected area electron diffraction patterns (SAEDs) indexing. TEM images were recorded using a dedicated CCD camera.

Microhardness was measured by Vickers methods, according to standard ASTM E384 (8), with a Vickers Paar MHT-4® micro-indenter and load of 0.05 N for 10 seconds holding time.

Hardness was measured by Brinell methods, according to ASTM E18 (9), with Emco test Automatic M4U 025®, using a load of 62.5 N.

Nitrogen and oxygen analyses were carried out using LECO TC400 machine®.

2.3 Results and Discussion

2.3.1 Cryomilling with BPR 4:1

2.3.1.1 Densification of the Powder

Relative densities of the atomized and milled sintered specimens are shown in Table 1.

Table 1: Archimedes densities of the atomized and 20h sintered samples at three temperatures.

	Archimedes density (%)		
	350°C	450°C	525°C
	60MPa	60MPa	60MPa
Atomized	93.44	99.42	99.96
Milled 20h BPR 4:1	93.85	97.10	98.50

At 350°C, densities of the samples are low. At sintering temperature of 450 and 525°C, atomized samples almost achieve full density (> 99.4%) and milled samples reach around 97% and 98.5% of density, respectively. Table 2 and Table 3 present hardness and microhardness of the atomized and milled sintered samples.

Table 2: Hardness of the atomized and 20h sintered samples at three sintering temperatures.

	Hardness (HB62.5)		
	350°C	450°C	525°C
	60MPa	60MPa	60MPa
Atomized	43 ±1	70 ±0.1	72 ±0.1
Milled 20h BPR 4:1	68 ±1	71 ±0.1	73 ±0.1

Table 3: Microhardness of the atomized and 20h sintered samples at three sintering temperatures.

	Microhardness (HV0.05)		
	350°C	450°C	525°C
	60MPa	60MPa	60MPa
Atomized	92 ±1	126 ±2	118 ±3
Milled 20h BPR 4:1	98 ±3	133 ±2	119 ±2

At sintering temperature higher than 450°C, the hardness of the samples is similar for both specimens. These results show that there is no significant difference on the structure of the atomized and milled samples, due to grain growth in the milled samples generated by poor thermal stability reported in chapter 1. The microhardness decreases at 525°C for milled sample. It is again related with the grain growth.

Considering density, micro- and hardness results, next experiments will be carried out at 525°C under 60 MPa.

2.3.2 Cryomilling with BPR 32:1

2.3.2.1 Densification of the Powder

Figure 3 shows the SPS curves for 8h milled not degassed powder. The powder was sintered at 525°C under 60 MPa.

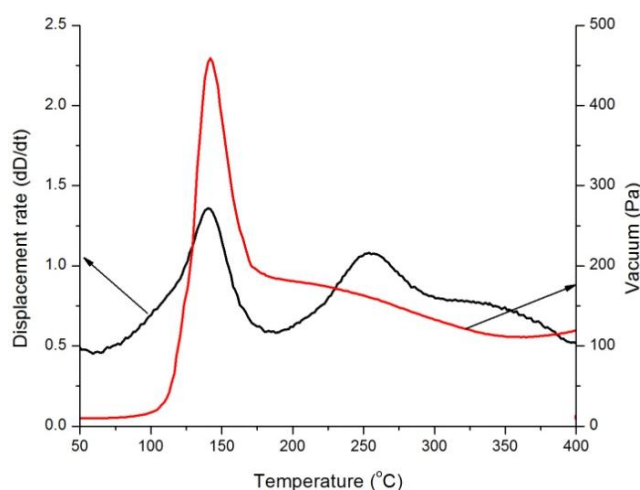


Figure 3: SPS curve sintered at 525°C under 60 MPa of the 8h cryomilled and not degassed sample.

The displacement rate presents two peaks. The first peak, which is around 140°C, corresponds to rearrangement of the particles and the expulsion of the gas adsorbed on particle surfaces during heating (degassing of the powder *in situ*), which finds a correspondence in the peak of the vacuum at the same temperature. At this moment, samples show no evidence of sintering (10). The second peak, which is around 260°C, corresponds to

the densification process where the powder was compacted. The formation of the necks between the particles starts due to discharge between small contact areas of the particles. After that, the contact between the particles starts to increase (11).

Figure 4a and b show SPS curves for 8h cryomilled powders and degassed at 250 and 350°C, respectively.

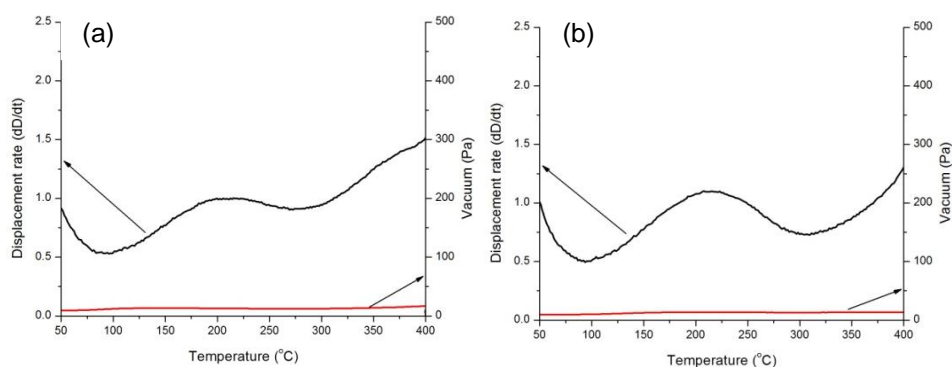


Figure 4: SPS curves of the 8h milled samples and degassed at (a) 250°C and (b) 350°C for 20h. Powders were sintered at 525°C with 60 MPa of pressure.

There is no degassing and vacuum remains on the initial level during whole cycle. In fact, the gas adsorbed on powder surface is removed during degassing. The degassing process before sintering is essential to facilitate the sintering process, to reach high density and desirable microstructure.

Archimedes densities of sintered samples are shown in Table 4.

Table 4: Archimedes density of the atomized and 8h milled samples sintered at 525°C under 60 MPa.

	Degassing	Archimedes density (%)
Atomized	--	99.96
	--	86.94
Milled 8h BPR 32:1	250°C 20h	97.87
	350°C 20h	97.93

Atomized sample achieves full density (> 99.9%). Milled sample reaches low density, around 87%. Contrarily, milled degassed specimens almost achieve full density, around 98%.

Table 5 and Table 6 report the hardness and the microhardness of the atomized and milled samples.

Table 5: Hardness of the atomized and 8h milled sintered samples.

	Degassing	Hardness (HB62.5)
Atomized	--	72 ±0.05
	--	77 ±0.15
Milled 8h BPR 32:1	250°C 20h	83 ±0.09
	350°C 20h	83 ±0.02

Table 6: Microhardness of the atomized and 8h milled sintered samples.

	Degassing	Microhardness (HV0.05)
Atomized	--	118 ±3
	--	133 ±4
Milled 8h BPR 32:1	250°C 20h	190 ±6
	350°C 20h	188 ±5

Despite of grain growth occurring on degassing, hardness and microhardness of the degassed sintered samples are higher than those of the atomized one, because of the finer structure.

2.3.2.2 Impurities in the Sintered Sample

Table 7 shows the amount of nitrogen and oxygen in sintered samples using as-atomized powder, as-milled one and two degassed ones.

Table 7: The amount of the nitrogen and the oxygen containing in atomized, 8h cryomilled and degassed samples.

	Degassing	N₂ (%)	O₂ (%)
Atomized	--	0.002	0.207
	--	4.330	11.120
Milled 8h BPR 32:1	250°C 20h	0.001	0.541
	350°C 20h	0.002	0.220

The amount of gases in atomized and 8h degassed sintered samples is low. Contrarily, a high quantity of nitrogen and oxygen gases was found on milled sintered sample.

2.3.2.3 Characterization of the Sintered Sample

Figure 5 shows SEM images of atomized and milled sintered samples.

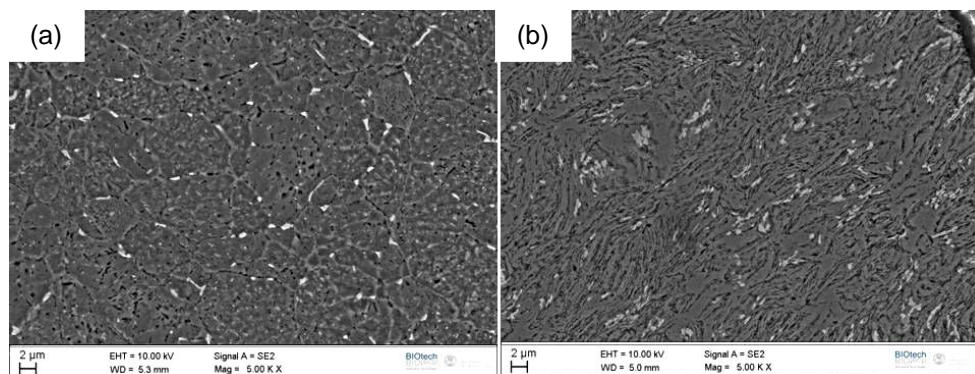


Figure 5: SEM analyses of (a) atomized and (b) 8h milled sintered sample.

Atomized sintered sample displays equiaxed grains and several larger precipitates at grain boundaries and finer intragranular precipitates (see Figure 5a). Milled sintered sample shows residual micropores and precipitates, in which some of them are agglomerated. Grains are not visible because of the residual deformation, as shown the Figure 5b.

Figure 6 shows SEM micrographs of the 8h cryomilled degassed sintered samples.

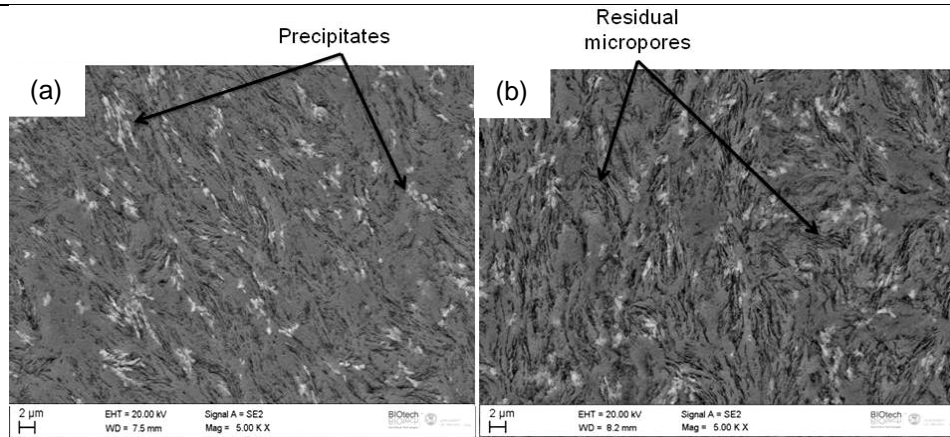


Figure 6: SEM image of the 8h cryomilled samples and degassed at (a) 250°C and (b) 350°C for 20h.

Micrographs are similar; residual micropores and precipitates are still visible, as well as the residual deformation. No differences between the milled degassed sintered microstructures are observable.

TEM analyses were carried out on degassed sintered samples. Crystallites present a bimodal distribution with ultra-fine grained (UFG) and micrometric zones. Bimodal microstructure was explained by (12), when the copper particles were submitted to single-pulse discharges. Yahagisawa et al. (12) observed that the sparks were formed only between some particles. Consequently, bimodal distribution may take place due to the localized overheating resulted by the sparks.

Figure 7 shows grains that measure approximately 100 - 200 nm.

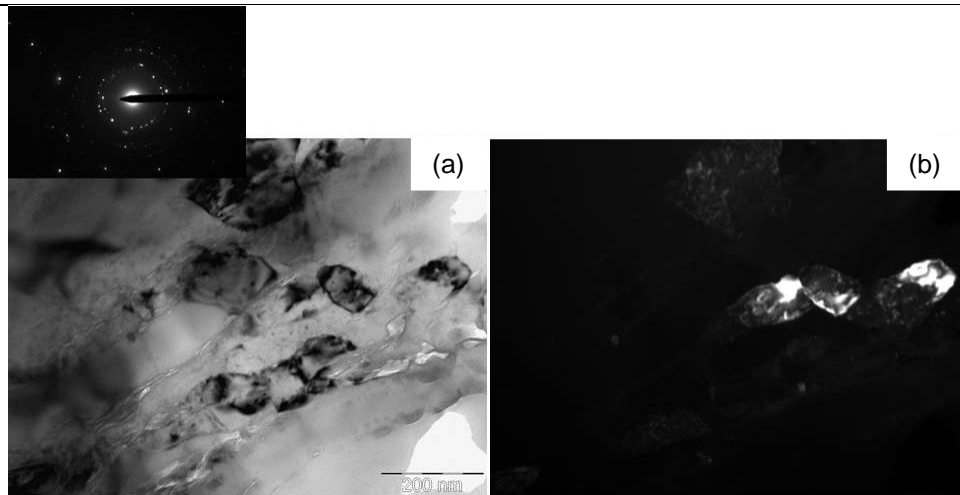


Figure 7: (a) BF with SAED pattern and (b) DF from TEM analysis of the 8h cryomilled samples degassed at 350°C for 20h .

Figure 8 shows ultra-fine zones without significant precipitation. The crystallites measure around 100 – 300 nm and the nanopores are tendentially distributed at the grain boundaries. There is no difference between degassed samples.

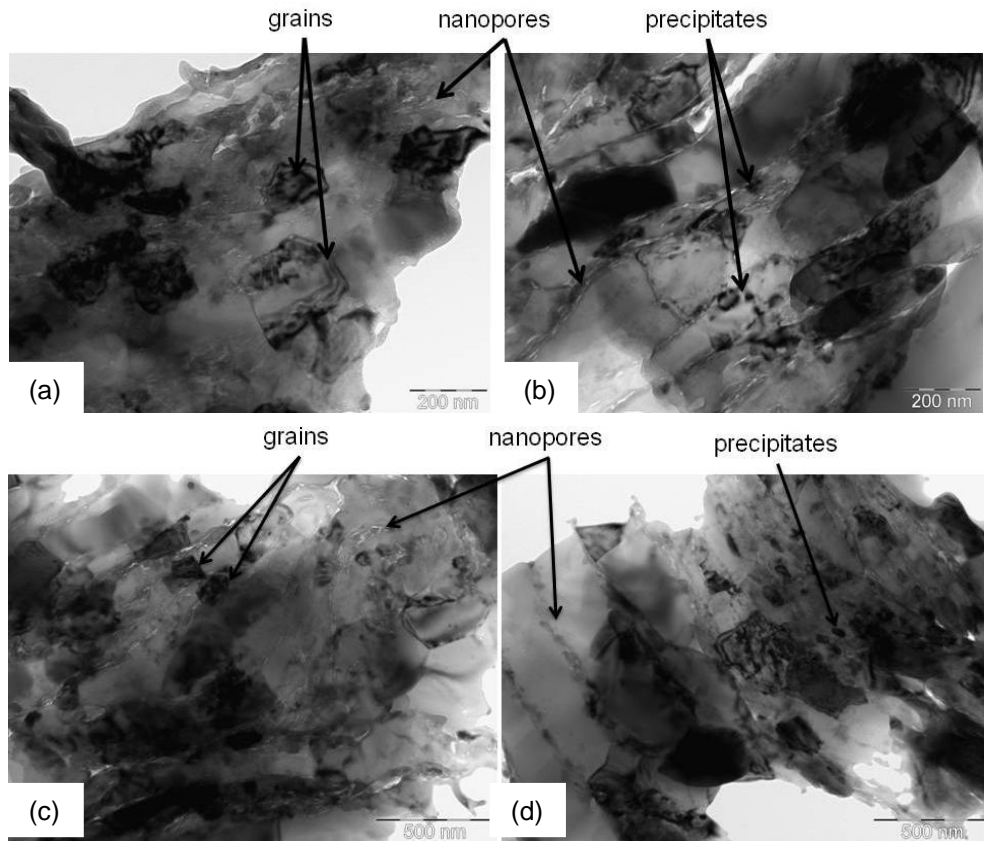


Figure 8: TEM images of the 8h cryomilled and degassed sample (a), (b) at 250°C and (c), (d) at 350°C for 20h.

TEM images in Figure 9 show the BF and SAED pattern of 8h milled sample and degassed at 250°C.

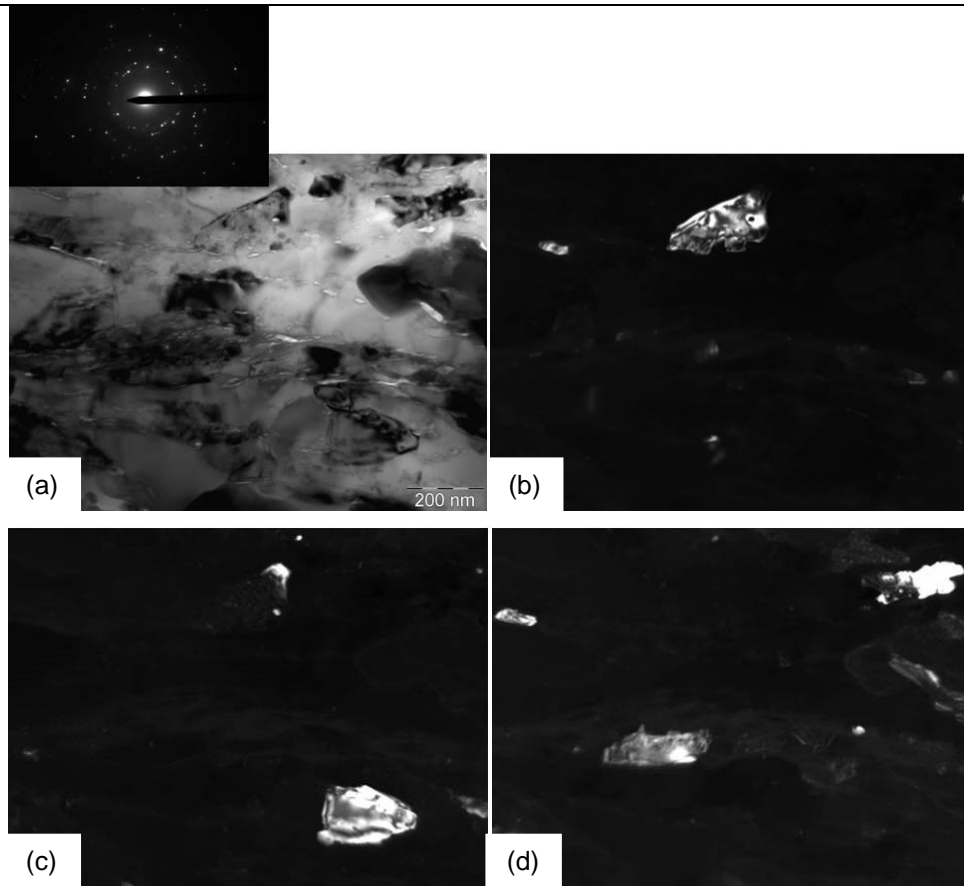


Figure 9: (a) BF, SAED pattern and (b), (c), (d) DF from TEM images of 8h cryomilled sample and degassed at 250°C for 20h.

Figure 9 shows crystallites which measuring around 100 - 200 nm. Micrometric zone contains precipitates distributed within the grains: rounded θ phase and elongated S phase (13), as show the Figure 10. The precipitates measure around 20 – 200 nm and they are shown in finer details.

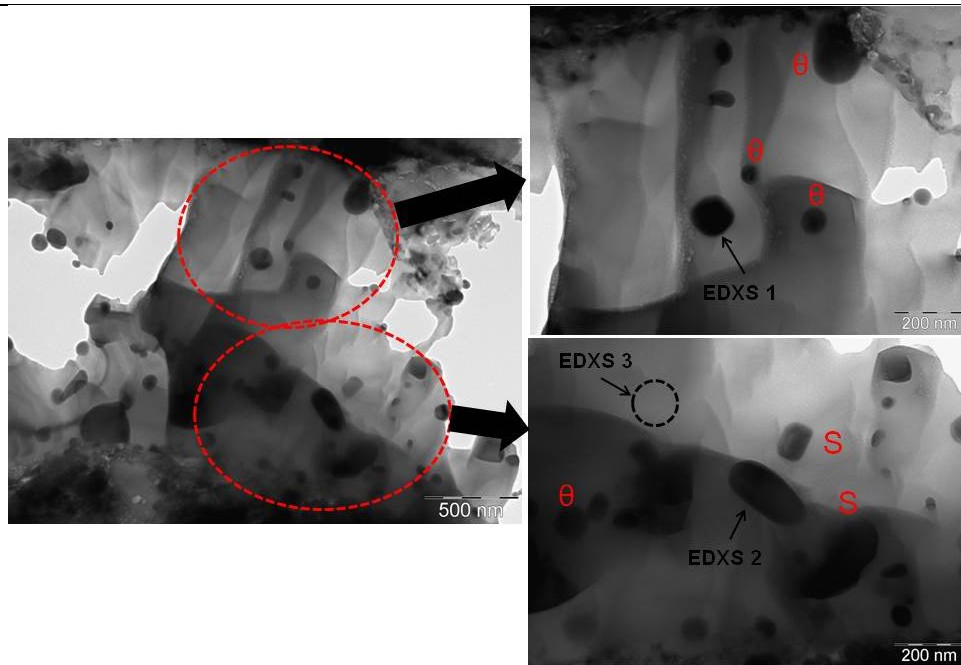


Figure 10: TEM analyses show θ and S precipitates of the 8h cryomilled sample and degassed at 250°C for 20h.

EDXS microanalyses (see Figure 11) confirm the chemical composition of the θ phase (Al_2Cu), S phase (Al_2CuMg) and matrix as indicated by EDXS 1, 2 and 3, respectively, in Figure 10.

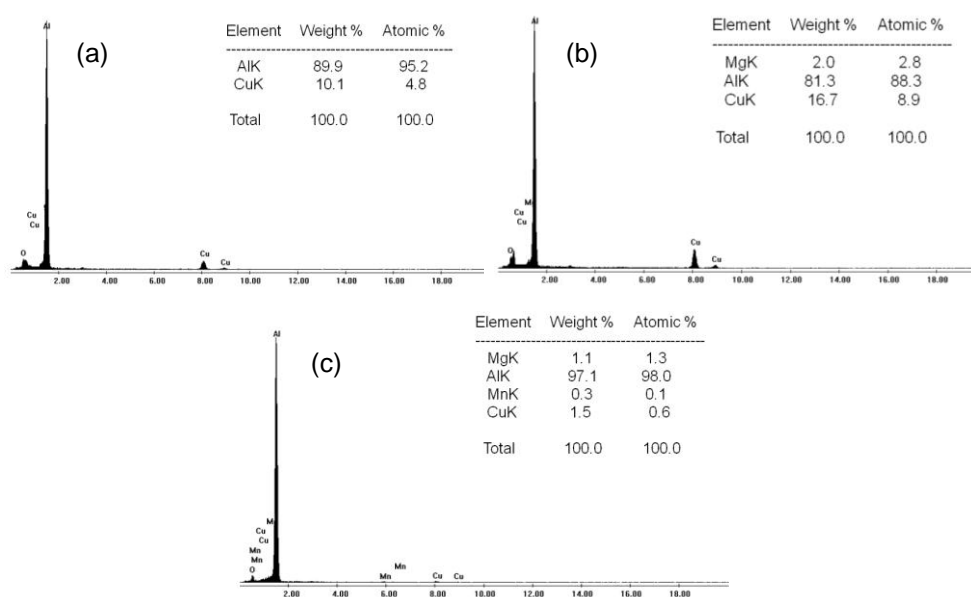


Figure 11: EDXS microanalyses exhibit the chemical composition of (a) θ and (b) S phases and (c) matrix.

As mentioned in the chapter 1, during milling the powder in contact with the liquid nitrogen forms some impurities (AlN). The Figure 12 shows the AlN particles formed into the grains.

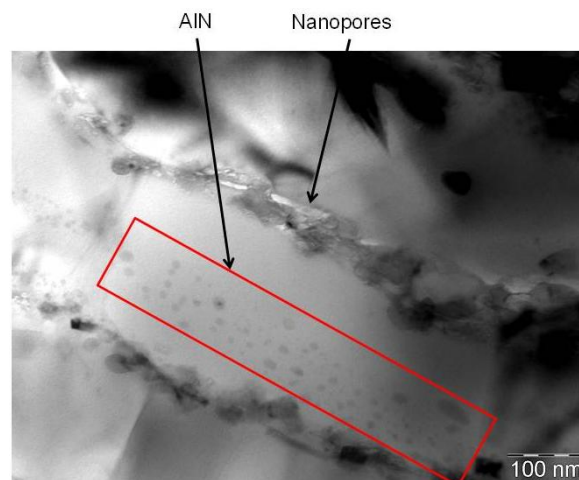


Figure 12: TEM image shows AlN and nanopores of the milled sample and degassed at 350°C for 20h. The sintering was carried out at 525°C with 60 MPa.

Since the results of degassed samples at 250 and 350°C are similar, the degassed specimen at lower temperature (250°C) is selected to carry out the hot compression tests.

2.4 Summary

Ultra-fine grained/micrometric 2024 aluminium alloy samples are produced using spark plasma sintering (SPS) technique with different temperatures. Atomized sample achieves full density at high sintering temperature (525°C) and pressure (60 MPa). Densities are low for milled samples not degassed powders. On the other hand, densities are close to full density (~98%) for powders degassed and sintered at 525°C and 60 MPa of pressure.

Hardness and microhardness of milled degassed sintered samples are higher than those of the atomized one. The structure of milled samples displays a bimodal ultra-fine grain in range of 100 – 300 nm and micrometric zones. The material contains grain boundary nanopores, very fine AlN precipitates and rounded θ (Al_2Cu) and elongated S (Al_2CuMg) phases. EDXS microanalyses confirm the chemical composition of matrix, θ and S phases.

A near full density 2024 Al alloy with a bimodal structure in the UFG/micrometric range can be obtained by the following processing route:

- cryomilling with BPR of 32:1 for 8 hours;
- degassing at 250°C for 20 hours;
- sintering by SPS at 525°C with 60 MPa.

Despite of grain growth occurring on degassing and sintering, the material maintains a structure in the UFG/micrometric range.

REFERENCES

- (1) R.Orru, R.Licheri, A.M.Locci, A.Cincotti, G.Cao. 2009, *Materials Science and Engineering A*, Vol. 63, pp. 127-287.
- (2) K.A.Khor, K.H.Cheng, L.G.Yu, F.Boey. 2003, *Materials Science and Engineering A*, Vol. 347, pp. 300-305.
- (3) X.Song, X.Liu, J.Zhang. 2006, *Journal of American Ceramic Society*, Vol. 89, pp. 494-500.
- (4) T.Mizuguchi, S.Guo, Y.Kagawa. 2010, *Ceramics International*, Vol. 36, pp. 943-946.
- (5) M.Tokita. Sumitomo Cal Mining Company, Ltd. Internal Communication, p. 13.
- (6) M.Kubota. 2007, *Journal of Alloys and Compounds*, Vols. 434-435, pp. 294-297.
- (7) ASTM B962-08. Density of Compacted or Sintered Powder Metallurgy (PM) Products Using Archimedes Principle 1.
- (8) ASTM E384-09. Standard Test Method for Microindentation Hardness of Materials.
- (9) ASTM E18-08b. Standard Test Methods for Rockwell Hardness of Metallic Materials.
- (10) U.Anselmi-Tamburini, J.E.Garay, Z.A.Munir, A.Tacca, F.Maglia, G.Spinolo. 2004, *Journal of Materials Research*, Vol. 19, pp. 3255-3262.

- (11) I.Lonardelli. *PhD Thesis*. April 2010. pp. 1-111.
- (12) O.Yanagisawa, H.Kuramoto, K.Matsugi, M.Komatsu. 2003, *Materials Science and Engineering A*, Vol. 350, pp. 184-189.
- (13) G.R.Ebrahimi, A.Zarei-Hanzaki, M.Haghshenas, H.Arabshahi. 2008, *Journal of Materials Processing Technology*, Vol. 206, pp. 25-29.

CHAPTER 3

HOT DEFORMATION BEHAVIOUR OF THE BIMODAL ULTRA-FINE GRAINED/MICROMETRIC ALLOY

3.1 Hot Workability

Hot workability is typically defined as the amount of plastic deformation that a material can undergo at a given strain rate and temperature, without fracture or flow localization and achieving a desirable deformed microstructure (1) (2). The high temperatures result in different microstructural phenomena that significantly influence hot workability and through the final microstructure, the mechanical properties of the material (3).

If the temperature of deformation is high enough, the flow stress is significantly reduced due to dynamic recovery and to dynamic recrystallization (4). During deformation, new crystallites are dynamically developed even in Al alloys with high stacking fault energy. The high stacking fault energy can generate the annihilation and rearrangement of

dislocations (recovery) and recrystallization (either dynamic or meta-dynamic). The energy is stored into the material mainly in the form of dislocations and is released through recovery and recrystallization, eventually followed by grain coarsening (5) (6) (7). Recrystallization is important in the processing of metallic alloys for two main reasons: it decreases hardness and restores the ductility of strain hardened material by creating a new structure by nucleation and growth of undeformed grains and controls the crystallite grain size of the final product (8). Dynamic recovery is also an important mechanism during hot deformation of Al alloys (6), since it contributes to the recovery of some mechanical properties of the deformed metal, which becomes similar to the undeformed one. In general, this process occurs at temperature at which dislocations have enough mobility and the rate of dislocation removal is equal to their production. The recovery kinetics depends on the size and distribution of secondary phase particles. Grain coarsening is the growth of the mean grain size driven by the reduction in grain boundary surface area. Coarsening can take place either by 'normal' grain growth, whose main mechanism is the growth of the large grains at the expenses of the small ones, or by 'abnormal' grain growth, which involves the growth of a few grains which become much larger than the average (8).

The optimum working conditions are defined in terms of a "processing window", which is defined as the range of temperature and strain rate where workability results in the optimum microstructure. For a given material the processing window is conventionally established on the basis of workability parameters, such as efficiency of power dissipation, flow localization parameter, instability criteria, tensile ductility, apparent activation energy and/or existence of favourable microstructural

mechanisms as dynamic recrystallization, dynamic recovery or superplasticity (9). The temperature of hot working influences the velocity of the process and depends on the heating due to internal shear, tool-material interface friction and heat transfer and initial temperature of material. The speed of the process is also affected by strain rate that significantly influences flow stress (10).

Mechanical properties of the materials are subject to local changes that lead to defects and internal stress in work piece. Furthermore, the dynamic restoration mechanisms, associated with hot working operations and workability, are strongly influenced by the local variations of temperatures and strain rates (10).

3.1.1 Strain Rate Sensitivity

Strain rate sensitivity (m) of metals and alloys deformed at high temperature is an important parameter to determine the flow stress in forming processes (11). Its definition is based on incremental changes in strain rate during tests performed at a fixed temperature and microstructure, to determine corresponding changes in flow stress (12).

Strain rate sensitivity is defined as the slope of the curve $\ln(\sigma)$ vs. $\ln(\dot{\epsilon})$ and it is given by equation 1 (5) (13) (14).

$$m = \frac{\delta \ln(\sigma)}{\delta \ln(\dot{\epsilon})} \quad (1)$$

where σ is the true flow stress and $\dot{\epsilon}$ is the true strain rate.

3.1.2 Processing Map

Processing map is a representation of the response of a material, in terms of microstructural mechanisms, to the imposed parameters (temperature and strain rate) and consists in a superimposition of a power dissipation map and an instability map (15). The processing map is used to understand the hot workability of many materials in terms of microstructural processes operating over a range temperature and strain rate. This technique is based on the dynamic materials model (DMM) in which the complementary relationship between the rate of generation of visco-plastic heat induced by deformation and the rate of energy dissipation associated with microstructural changes during deformation are considered.

One of the requirements for process modelling is knowledge of the material flow behaviour for defining deformation processing maps that define safe and unsafe hot working conditions. These maps show the processing conditions for stable and unstable deformation in dependence of temperature and strain rate (2).

During deformation, power dissipation occurs through temperature rise (called G content) and microstructural change (called J content) of the work piece material. In general, most of dissipation is due to a temperature rise, and only a small amount of energy is dissipated through microstructural changes (13). The power (P), per unit volume, absorbed by the work piece material during flow is given by:

$$P = G + J \quad (2)$$

where G is the dissipater content and J is the dissipater co-content (2). The G term represents the power dissipated by plastic work and J is related to metallurgical mechanisms which occur dynamically to dissipate power (see Figure 1) (2).

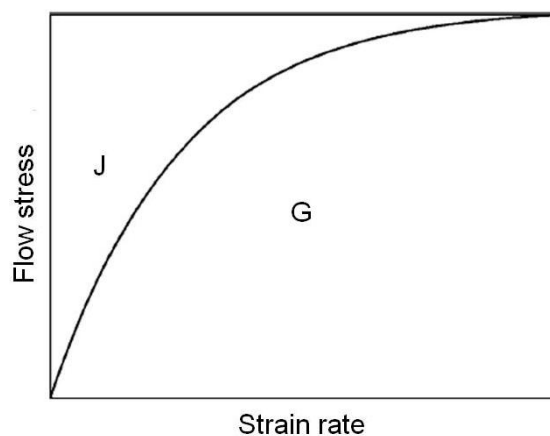


Figure 1: Schematic representation of stress – strain rate curve showing the areas corresponding to G and J (2).

Metallurgical processes such as dynamic recrystallization, dynamic recovery, internal fracture, dissolution or growth of particles or phase under dynamic conditions, etc, contribute to the changes in the dissipated power co-content (J) (2).

A detailed description of the procedure used for the determination of the power dissipation map, as well as of the instability conditions is reported in the following sections where the results of the tests carried out are presented.

It is well known that the most properties of solids depend on their microstructure. The grain size in a material has substantial effects on physical and mechanical properties. In general, ductility and strength of materials are correlated to defects and microstructures of the polycrystalline materials. An increase in strength can be achieved introducing microstructural barriers to dislocation motion. These barriers can be second-phase particles, solid solution atoms and the rise of the grain boundary volume fraction with decreasing crystallite size. The comprehension that a material with high density of grain boundaries is stronger than a coarse-grained material with low density of grain boundaries is described by Hall-Petch relationship (H-P) (16):

$$\sigma_y = \sigma_0 + k_y D^{-\frac{1}{2}} \quad (3)$$

where D is the mean grain size, σ_y the yield strength, σ_0 is the yield strength of the same material with infinite grain size and k_y is the material constant.

This relation is always obeyed for ductile metals with crystallite size in the micrometric range, ultra-fine crystallites (100 - 300 nm) or nanometric grains (30 -100 nm). Below this limit, there are uncertainties regarding the effective softening trend that is reported by (11) (17).

Nanostructure influences the hot workability, as well. An important characteristic of the deformation behaviour of nanomaterials is high strain rate sensitivity (m), even at low temperatures (18) (19) (20). Literatures provide experimental results of m as a function of crystallite size for nano-, ultra-fine- and microcrystalline metals and alloys (21) (22). It is known that a reduction in grain size from micro- to nanocrystalline regime increases

the strain rate sensitivity of plastic deformation of most FCC materials in an order of magnitude. Normally, an increase in m value is correlated to a change in basic deformation mechanism from intragranular dislocation mechanisms to grain boundary sliding and transition of the material to a superplastic state in terms of rate-controlling mechanism (20).

The activation volume, which is defined as the rate of decrease of activation enthalpy with respect to flow stress at fixed temperature and which influences the rate-controlling mechanisms in the plastic deformation of metals and alloys, is some two orders of magnitude smaller for nano- than for microcrystalline metals (23) (24). The large quantity of grain boundaries provides barriers to dislocation motion during plastic deformation and generally it leads to increased strength in nanograin metals. However, twin boundaries (which are special kinds of coherent internal interfaces) also impede the dislocation motion. Recent experiments show that the introduction of nano-scale twins within ultra-fine crystalline metals leads to considerable increases in hardness and flow stress (23) (25). The extent of such strengthening is comparable to that achievable by nanograin refinement. The inclusion of nano-scale twins during the processing of metals with ultra-fine grains is also known to enhance the loading rate sensitivity by almost an order of magnitude and decrease the activation volume by two orders of magnitude as compared to the values observed in microcrystalline metals (21) (23).

3.2 Experimental Procedures

3.2.1 Hot Deformation Tests

Hot deformation tests of atomized and 8h milled, degassed and sintered specimens were performed in a Baehr Dilatometer 805 A/D equipped with a compression head.

SPS disks (20 mm of diameter and ~ 6.5 mm of height) were cut into several cylindrical samples (see Figure 2) with 3 mm of diameter and 6 mm of height by Electro Discharge Machining (EDM). Samples were polished to produce parallel flat faces.



Figure 2: Specimen (a) before and (b) after hot compression test.

Samples were compressed at strain rates of 0.01, 0.1 and 1 s⁻¹ and temperatures of 300, 350 and 400°C.

Figure 3 shows temperature and true strain vs. time of the cycles imposed during hot deformation test.

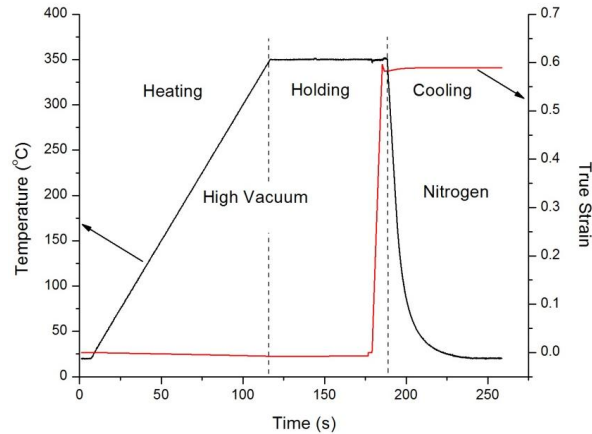


Figure 3: Temperature and true strain behaviour on hot deformation test carried out at 350°C and 0.1 s⁻¹.

During heating, the temperature increases up to a maximum value at a rate of 3°C/s. In order to homogenise the sample, the temperature was maintained for 60 seconds. After that, the strain was immediately applied and the cooling with nitrogen at 30°C/s was carried out in order to “freeze” the microstructure of the samples.

3.2.2 Microstructural Characterization

Microstructural characterization was carried out by means of Light Optical Microscopy (LOM), Scanning Electron Microscopy (SEM) and Transmission Electron Microscopy (TEM). Specimens were prepared with procedures described in chapter 2.

3.3 Results and Discussion

3.3.1 Hot Deformation of Atomized Sintered Alloy

Figure 4 shows true stress vs. true strain diagrams of atomized specimens deformed at different temperatures and strain rates.

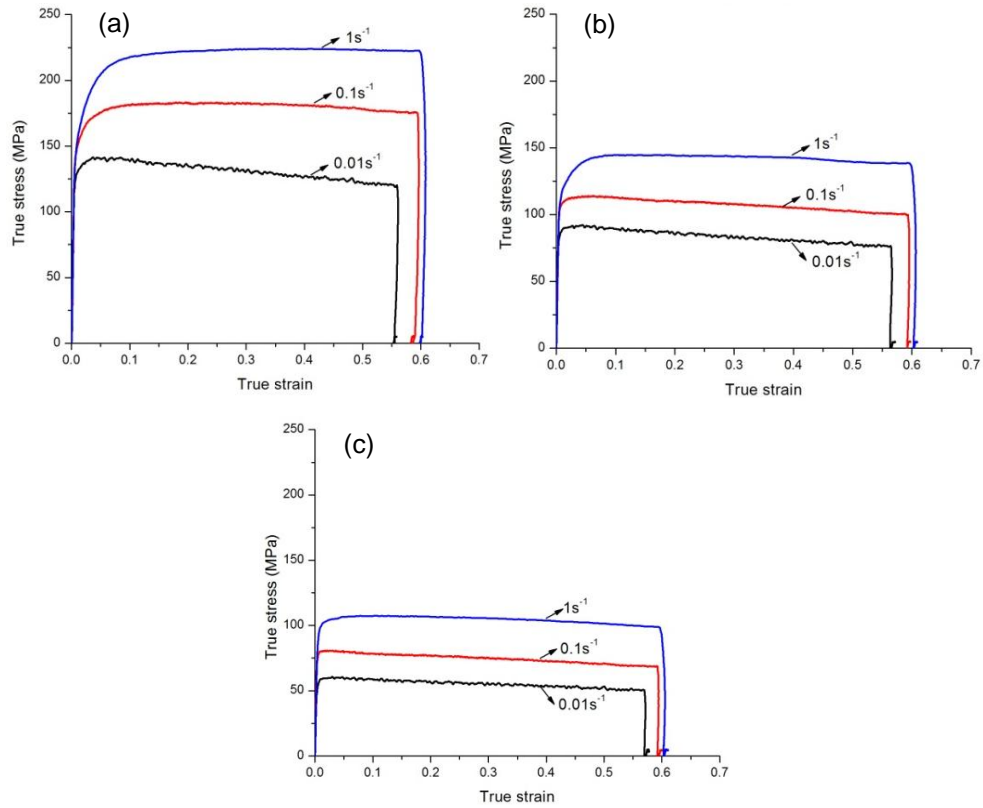


Figure 4: True stress – true strain curves of atomized sintered samples with strain of 0.6 and temperature of (a) 300°C , (b) 350°C and (c) 400°C .

Curves exhibit typical shape of Al-Cu-Mg alloys at temperature in the range 300 – 400°C and strain rates of 0.01 – 1 s⁻¹ (15) (26). All curves present direct relationship between flow stress and strain rate, i.e. on increasing the strain rate the flow stress increases.

Figure 4a shows true stress - true strain curves at 300°C:

- The flow stress at 0.01 s⁻¹ suddenly raises up to maximum stress. Immediately after, the flow decreases slightly indicating a slight flow softening.
- Curves at 0.1 and 1 s⁻¹ show similar behaviour in which a steady state is attained after the maximum flow stress.
- The increase in stress to deform atomized alloy at 300°C from 0.01 to 1 s⁻¹ is 58%.

Figure 4b exhibits the curves at 350°C:

- Curves at 0.01 and 0.1 s⁻¹ are similar. The flow stress suddenly increases up to the maximum stress. After that, the flow stress slightly decreases indicating a slight flow softening.
- At strain rate of 1 s⁻¹, the maximum is reached more gradually. After that, the flow stress exhibits a slightly flow softening.
- The increase in stress to deform atomized alloy at 350°C from 0.01 to 1 s⁻¹ is 57%.

Figure 4c shows curves at 400°C:

- They present similar behaviour. Flow stress promptly increases up to maximum stress. After that, the flow stress exhibits slight softening.
- The increase in stress to deform atomized material at 400°C from 0.01 to 1 s⁻¹ 75%.

In case of curves that present steady state, dynamic recovery and work hardening are in equilibrium due to the flow stress remains almost

constant during the whole test. Generally, the work hardening is induced by dislocations multiplication and interaction (26).

Flow softening presented in several curves is mainly caused by either dynamic recovery and recrystallization into the material (26) (27) or adiabatic heating. It is well know that dynamic recovery can easily occur before dynamic recrystallization in Al alloys due to high stacking fault energy. On the other hand, dynamic recovery consumes the mass of dislocation and stored deformation energy inhibit dynamic recrystallization during hot compression tests, especially at low strain rate because this results in enough time for the dynamic recovery to consume the stored energy (26).

Figure 5 reports true stress vs. true strain curves at different temperatures of the atomized samples.

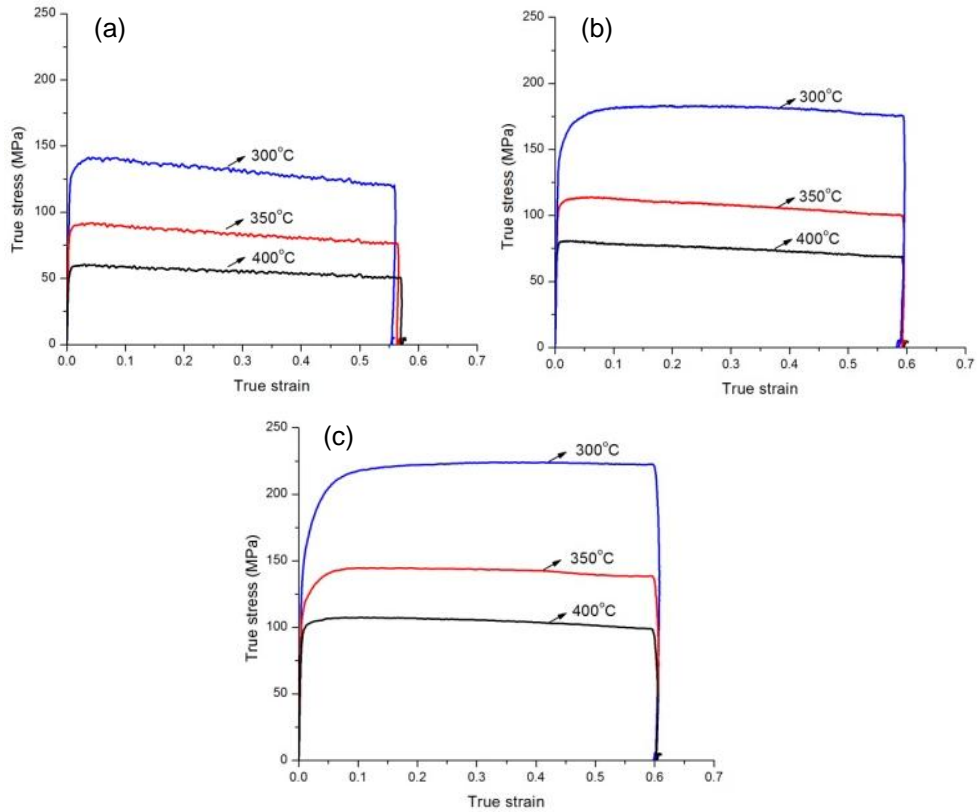


Figure 5: Hot compression tests with strain rate of (a) 0.01, (b) 0.1 and (c) 1 s^{-1} of the atomized samples.

On increasing the temperature the stress decreases, in particular from 300°C to 350°C. The flow process is strongly influenced by temperature and strain rate (26).

3.3.1.1 Relative Work Softening

Relative work softening (RS) is calculated in order to quantify the work softening in hot compression tests. It is given by equation 4 (28).

$$RS = \frac{\sigma_p - \sigma_{p+0.25}}{\sigma_p} \quad (4)$$

where σ_p is the peak stress and $\sigma_{p+0.25}$ is the stress at 0.25 strain after peak.

The relative work softening of the atomized samples is shown in Figure 6.

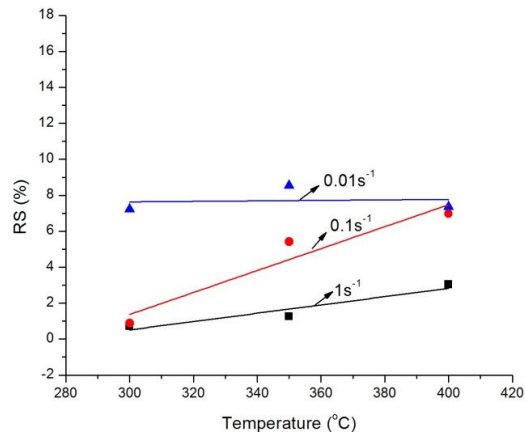


Figure 6: Percentage of work softening versus temperature of the atomized specimens.

Relative work softening at 300°C with strain rate of 0.1 and 1 s⁻¹ is equal. The same condition occurs at 400°C with 0.01 and 0.1 s⁻¹. On the other hand, RS values at 350°C increases on decreasing strain rate. The mean value of RS at 0.01 s⁻¹ is slightly constant with the temperature. At 0.1 and 1 s⁻¹, relative work softening increases on increasing the temperature.

3.3.1.2 Strain Rate Sensitivity

Figure 7 shows the $\ln(\sigma)$ vs. $\ln(\dot{\epsilon})$ and the slope is the strain rate sensitivity of the atomized samples.

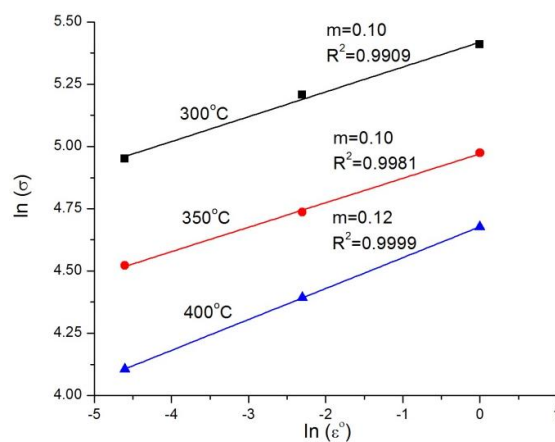


Figure 7: Strain rate sensitivity of atomized samples at three hot deformation temperatures.

Strain rate sensitivity is positive and slightly influenced by temperature. At 300 and 350°C, the m presents identical values. At 400°C m is higher, meaning a tendency to a more homogeneous deformation of the alloy.

Values found for atomized samples are from 0.10 to 0.12. They are lower than that reported in literature (29) which is 0.17 at 430°C for the 2024 Al alloy.

3.3.1.3 Processing Map

The approach of processing map is described in this study to represent and analyse the constitutive behaviour of the 2024 Al alloy during hot deformation tests. A power dissipation map represents the pattern in which the power input ($\sigma \times \dot{\epsilon}$) is dissipated by the material through microstructural changes rather than adiabatic heating (30).

It is well known that during deformation, power dissipation occurs by an increased temperature of the work piece material. In general, most of dissipation is due to a temperature raise, and only a small amount of energy is dissipated through microstructural changes (13).

Table 1 shows peak flow stress values obtained from true stress vs. true strain curves (see Figure 4) of the atomized samples.

Table 1: Peak flow stress of atomized samples at different temperatures and strain rates.

Strain rate (s ⁻¹)	Peak flow stress (MPa)		
	300°C	350°C	400°C
0.01	141.28	92.05	60.70
0.1	182.58	114.01	80.84
1	223.63	144.69	107.49

Figure 8 shows the peak flow stress versus strain rate in logarithmic scale at three temperatures.

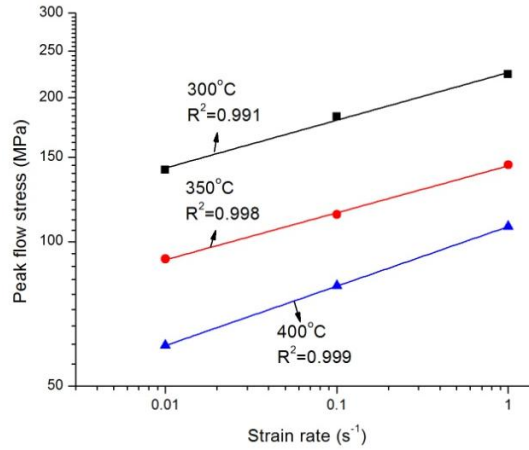


Figure 8: Peak flow stress and correlation factor of the atomized samples at three hot deformation temperatures.

Peak flow stress increases on decreasing temperature and increasing the strain rate.

A power dissipation map is constituted by variation of dimensionless parameter (η), called the efficiency of power dissipation, with temperature (T), strain (ϵ) and strain rate ($\dot{\epsilon}$) (2). The efficiency of power dissipation represents the relative rate of internal entropy produced during hot deformation and it characterizes the dissipative microstructure under different temperature and strain conditions (15).

The efficiency of power dissipation η is given by equation 5 (2) (15).

$$\eta = \frac{2m}{m + 1} \quad (5)$$

where m is the strain rate sensitivity.

The efficiency of power dissipation of the atomized samples is shown in Table 2.

Table 2: Efficiency of atomized samples hot deformed at three temperatures.

	300°C	350°C	400°C
Efficiency (η)	0.18	0.18	0.21

Results are in good agreement with the literature data (15).

3.3.1.4 Instability Map

The instability map may be superimposed on the power dissipation to obtain a processing map in which the limits for the unstable flow regime are clearly marked. This criterion is physically interpreted: if the material system does not produce entropy constitutively at given rate in match with the rate of entropy input through imposed process parameters, the flow becomes localized and causes flow instability (15).

The instability flow can be calculated according to Murty et al. (13), where the flow is stable if $0 < \eta < 2m$.

Table 3 shows $2m$ values.

Table 3: $2m$ values of atomized samples at three deformation temperatures.

	300°C	350°C	400°C
$2m$	0.20	0.20	0.24

In all cases, the stability condition presented by (13) is verified; consequently, the flow is stable in atomized samples.

Efficiency of power dissipation values as function of the temperature and the log of strain rate are reported in Table 4.

Table 4: Data of the efficiency contour map of the atomized samples.

log ($\dot{\epsilon}$)	η		
	300°C	350°C	400°C
-2	0.18	0.18	0.21
-1	0.18	0.18	0.21
0	0.18	0.18	0.21

Figure 9 shows the efficiency contour map of the 2024 Al alloy related by Prasad et al. (15) where experimental points calculated for atomized samples under hot deformation are included.

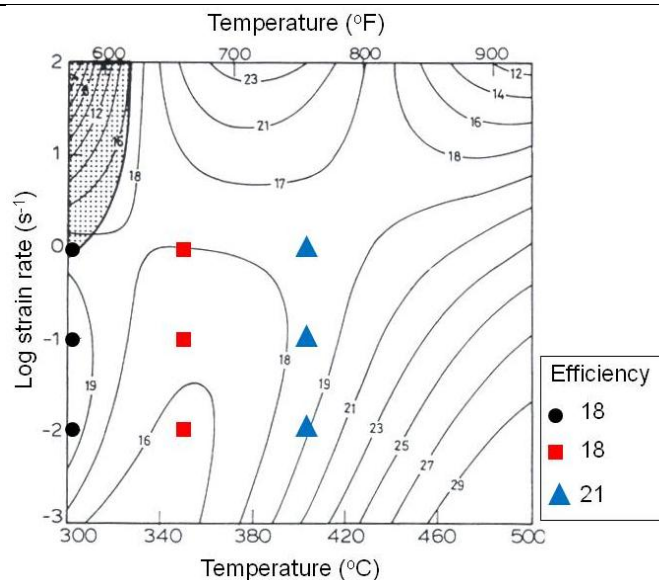


Figure 9: Efficiency contour map of the 2024 Al alloy (15) and experimental data of the atomized samples are added.

Results are in good agreement with Prasad data for 2024 Al alloy (15). The point at 300°C and 1 s⁻¹ should represent a condition of instability, which is not confirmed by the experimental results presented earlier. Atomized samples deformed at 300 – 400°C and strain rates in the range of 0.01 – 1 s⁻¹ present stability flow.

3.3.2 Hot Deformation of Milled Sintered Alloy

Figure 10 shows hot deformation curves of the milled, degassed and sintered samples at different temperatures and strain rates.

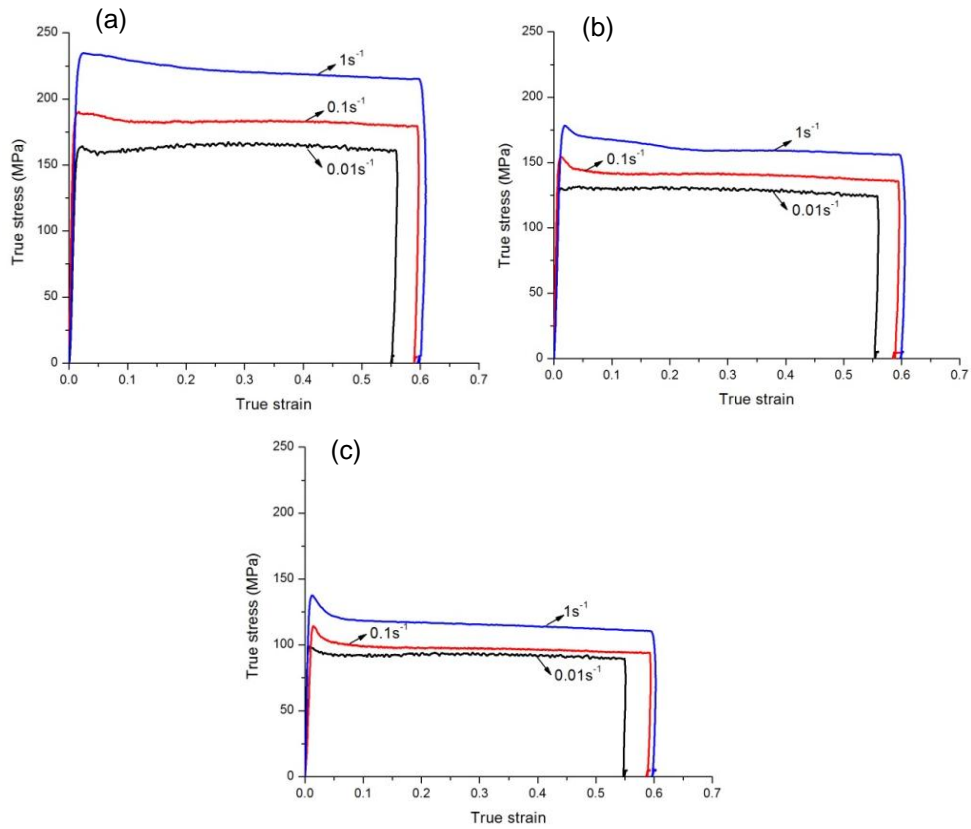


Figure 10: True stress – true strain curves of the milled samples with 0.6 of strain and temperatures of (a) 300°C , (b) 350°C and (c) 400°C .

Flow stress and strain rate have a direct relationship, i.e. on increasing the strain rate, the flow stress increases.

Figure 10a shows true stress – true strain curves at 300°C:

- At 0.01 s^{-1} , the curve exhibits a particular behaviour (see Figure 11). The flow stress quickly increases up to a peak flow stress. After that, the flow suddenly decreases until 0.04 of strain, displaying a sharp peak. The flow starts to rise again up to 0.3 of strain and then decreases. These phenomena characterize work hardening and flow softening, respectively.

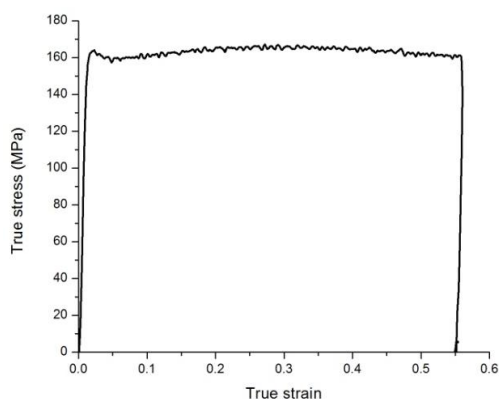


Figure 11: Hot compression of milled sample deformed at 300°C and 0.01 s^{-1} .

- Curves at 0.1 and 1 s^{-1} rapidly increase up to a peak stress. Immediately after, the flow stress slightly decreases up to the end of the deformation, exhibiting a slightly flow softening.

- The increase in stress to deform milled alloy under hot compression at 300°C from 0.01 to 1 s^{-1} is 41%.

Figure 10b shows curves at 350°C:

- The curve at 0.01 s^{-1} exhibits a particular behaviour. The flow stress increases quickly up to a maximum stress, but the sharp peak stress is not visible. After that, the stress reveals a slight flow softening.

- At 0.1 and 1 s^{-1} , the stress rapidly increases up to a peak stress. Immediately after, the flow stress abruptly decreases up to 0.04 of strain.

After that, the stress exhibits gradual flow softening up to the end of the deformation.

- The increase in stress to deform milled material at 350°C from 0.01 to 1 s⁻¹ is 36%.

Figure 10c shows the hot compression curves at 400°C.

- At 0.01 s⁻¹ the flow stress rapidly increases up to a peak stress. After that, it decreases revealing slightly flow softening.

- Curves at 0.1 and 1 s⁻¹ reveal identical behaviour. The flow stress quickly rises up to maximum stress and then suddenly decreases revealing a marked peak up to 0.04 of strain. After that, flow stress slightly decreases with a gradual flow softening.

- The increase in stress to deform milled alloy at 400°C from 0.01 to 1 s⁻¹ is 39%.

The peak flow stress at 0.1 and 1 s⁻¹ is always more evident than the peak at strain rate of 0.01 s⁻¹.

Figure 12 shows hot compression curves at three strain rates.

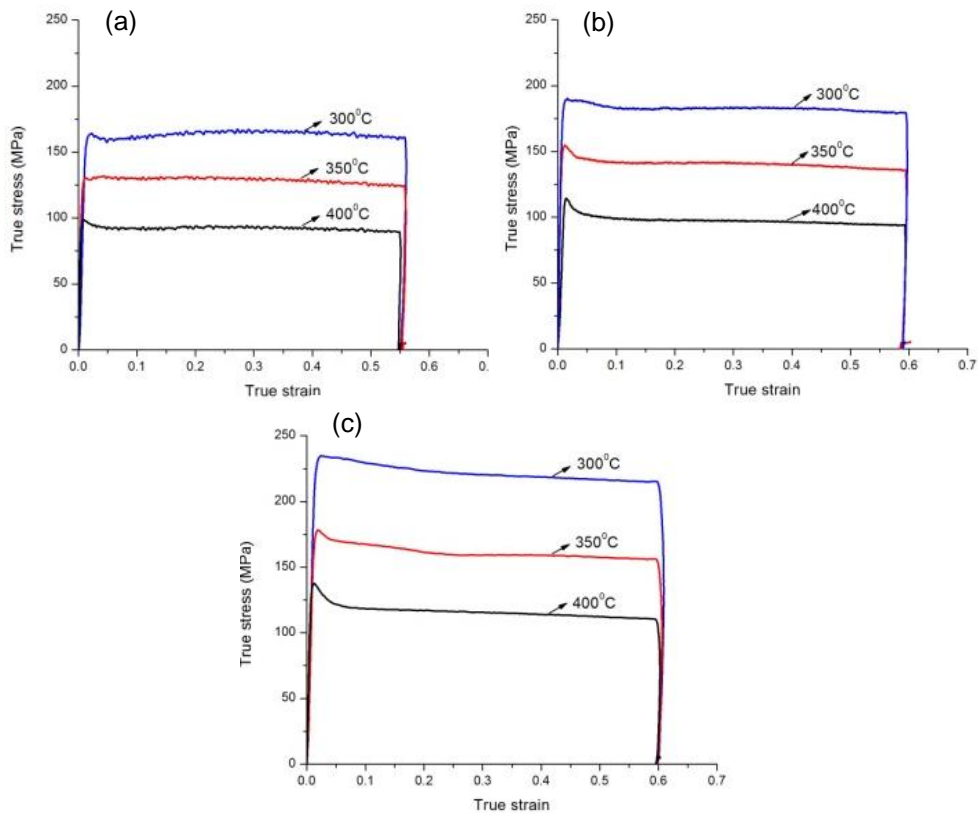


Figure 12: Hot compression curves at (a) 0.01, (b) 0.1 and (c) 1 s⁻¹ of milled samples.

The flow stress and consequently the peak flow stress increase on decreasing the temperature.

The increase in stress between 400°C and 350°C is identical to that between 350°C and 300°C. Curves exhibit slight flow softening at all temperatures, except for curve at 300°C and 0.01 s⁻¹, that exhibits work hardening and flow softening.

3.3.2.1 Relative Work Softening

Figure 13 shows the relative work softening of the milled samples.

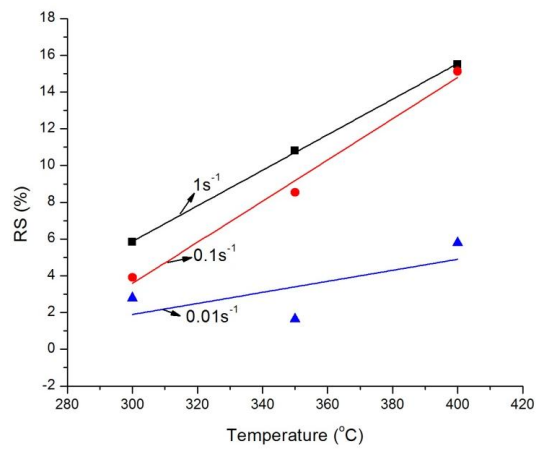


Figure 13: Relative work softening of the milled samples.

Relative work softening values at 400°C with strain rate of 0.1 and 1 s⁻¹ are similar. In all cases RS tends to increase with the temperature.

3.3.2.2 Strain Rate Sensitivity

Figure 14 shows $\ln(\sigma)$ vs. $\ln(\dot{\epsilon})$ and the slope is the strain rate sensitivity of the milled samples.

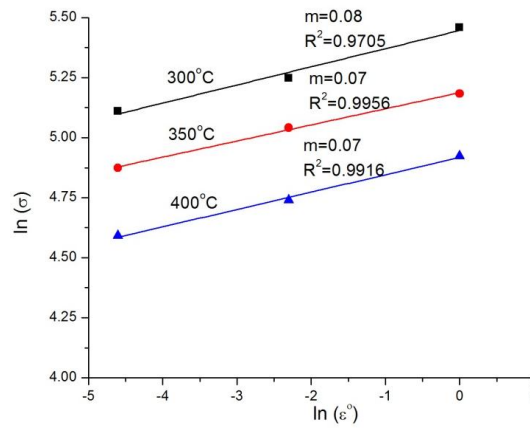


Figure 14: Strain rate sensitivity of the milled samples at three temperatures.

Strain rate sensitivity is slightly influenced by temperature. Values found here are 0.07 - 0.08, that are similar to reported by Hayes et al. (31) which found m of 0.08 - 0.15 at 149°C for UFG 5083 Al alloy obtained by cryomilling and hot isostatic pressing. Therefore for nanostructured 2024 alloy with crystallite size of 42 nm, the author found 0.01 which was obtained at room temperature (32).

3.3.2.3 Processing Map

Table 5 shows peak flow stress values of milled samples obtained from Figure 10.

Table 5: Peak flow stress of the milled samples at different temperatures and strain rates.

Strain rate (s ⁻¹)	Peak flow stress (MPa)		
	300°C	350°C	400°C
0.01	165.81	130.90	98.64
0.1	190.18	154.70	114.33
1	234.81	178.29	137.55

Figure 15 shows the peak flow stress versus strain rate in logarithmic scale at three hot compression temperatures.

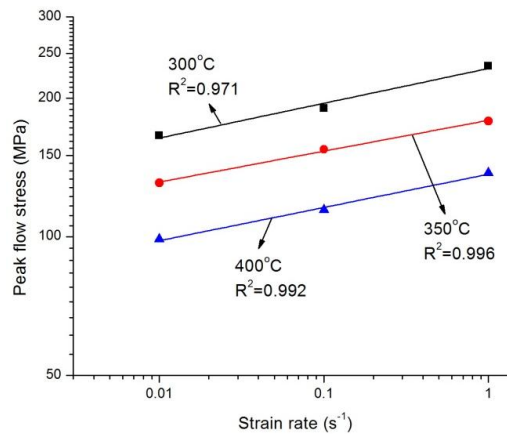


Figure 15: Peak flow stress of milled samples.

Peak flow stress increases on decreasing temperature and increasing the strain rate.

Table 6 shows the efficiency of power dissipation of the milled samples.

Table 6: Efficiency of milled samples at three deformation temperatures.

	300°C	350°C	400°C
Efficiency (η)	0.15	0.13	0.13

Efficiency values are in good match with literature data (15).

3.3.2.4 Instability Map

Table 7 shows $2m$ values of the milled hot compressed samples.

Table 7: $2m$ of milled samples at three hot deformation temperatures.

	300°C	350°C	400°C
$2m$	0.16	0.14	0.14

The stability condition presented by (13) is verified in all cases; consequently, the flow is stable in the milled samples.

In order to analyse the processing map, the efficiency of power dissipation (η) values as function of the temperature and the log of strain rate are shown in Table 8.

Table 8: Data for efficiency contour map of milled samples.

log($\dot{\epsilon}$)	η		
	300°C	350°C	400°C
-2	0.15	0.13	0.13
-1	0.15	0.13	0.13
0	0.15	0.13	0.13

Figure 16 shows the efficiency contour map of the 2024 Al alloy (15) with experimental data of the presented investigation.

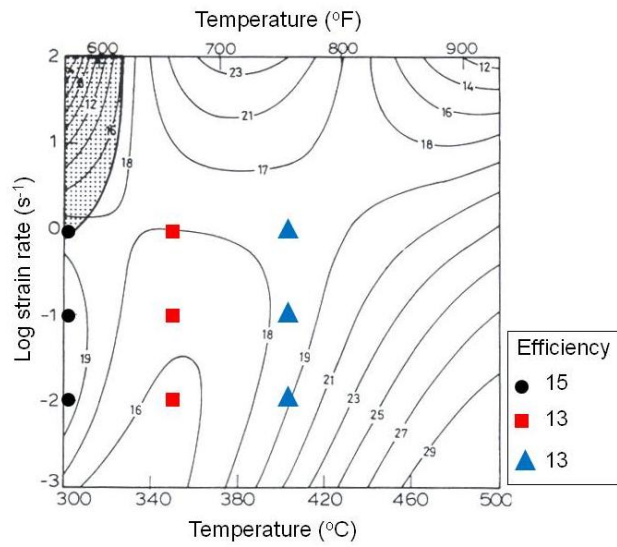


Figure 16: Efficiency contour map (15) and experimental data of the milled samples are added.

Results are in good agreement with Prasad data for 2024 Al alloy (15). Therefore, the sample hot compressed at 300°C and 1 s⁻¹ is localized in the instability field in the map.

The linear fit of $\ln - \ln$ plot for the calculation of the strain rate sensitivity is forced at 300°C, as shown by the correlation coefficient ($R^2 = 0.9705$). Another approach to verify instability was then used. Continuum instability criterion (ξ) is represented by equation 6 (13) (15) (30).

$$\xi(\dot{\epsilon}) = \frac{\partial \ln\left(\frac{m}{m+1}\right)}{\partial \ln(\dot{\epsilon})} + m < 0 \quad (6)$$

where m is the strain rate sensitivity and $\dot{\epsilon}$ is the true strain rate.

If $\xi = 0$, stable and unstable regions bifurcate in processing map. If $\xi < 0$ indicates microstructural instability and, finally if $\xi > 0$ implies microstructural stability in the material. Thus the variation of the instability parameter ξ with ϵ , $\dot{\epsilon}$ and T constitutes an instability map for delineating regimes of flow instability (2) (15) (30).

If the strain rate sensitivity does not change with strain rate, the term $\frac{\partial \ln\left(\frac{m}{m+1}\right)}{\partial \ln(\dot{\epsilon})}$ becomes zero and then the instability is verified just only if $m < 0$.

Figure 17 shows the $\ln(\sigma)$ vs. $\ln(\dot{\epsilon})$ of milled sample hot compressed at 300°C re-plotted in a polynomial fit.

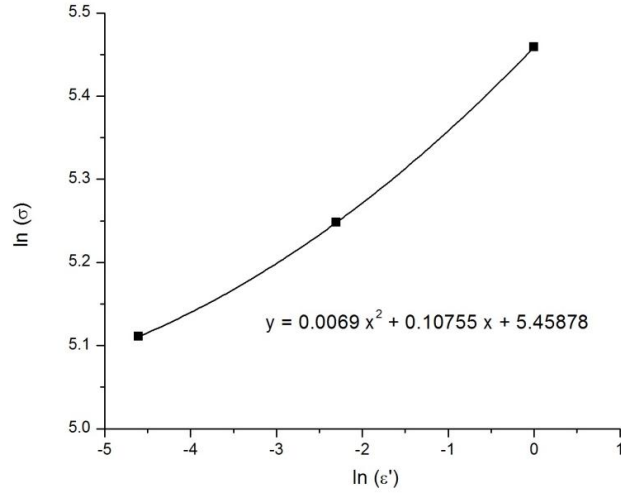


Figure 17: $\ln(\sigma)$ vs. $\ln(\dot{\epsilon})$ of the milled sample at 300°C and plotted by polynomial fitting.

The 'new' strain rate sensitivity is calculated as the first derivative of the polynomial fit.

Table 9 shows the terms $\ln(\dot{\epsilon})$ and $\ln\left(\frac{m}{m+1}\right)$ of the milled samples hot deformed at 300°C .

Table 9: Calculus of the instability criterion of milled specimens hot deformed at 300°C .

Milled samples hot deformed at 300°C			
$\dot{\epsilon}$	1	0.1	0.01
$\ln(\dot{\epsilon})$	0	2.30	-4.61
m	0.20	0.17	0.13
$\ln\left(\frac{m}{m+1}\right)$	-1.80	-1.95	-2.14

In order to calculate the instability criterion related by (15), $\ln\left(\frac{m}{m+1}\right)$ vs. $\ln(\dot{\epsilon})$ is plotted with data from Table 9, as show the Figure 18.

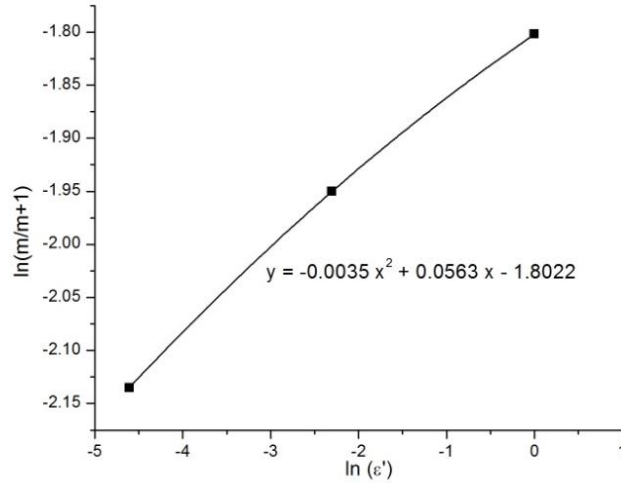


Figure 18: Plot of the instability criterion of the milled samples hot compressed at 300°C.

Deriving the equation given in Figure 18, the terms $\frac{\partial \ln\left(\frac{m}{m+1}\right)}{\partial \ln(\dot{\epsilon})}$ and $\frac{\partial \ln\left(\frac{m}{m+1}\right)}{\partial \ln(\dot{\epsilon})} + m$ for three $\ln(\dot{\epsilon})$ values are calculated, and the results are shown in Table 10.

Table 10: Instability criterion data of milled samples compressed at 300°C.

Milled samples hot deformed at 300°C			
$\ln(\dot{\epsilon})$	0	-2.30	-4.61
$\frac{\partial \ln\left(\frac{m}{m+1}\right)}{\partial \ln(\dot{\epsilon})}$	0.06	0.07	0.09
$\frac{\partial \ln\left(\frac{m}{m+1}\right)}{\partial \ln(\dot{\epsilon})} + m$	0.26	0.24	0.22

Results are positive, consequently $\xi > 0$ and milled samples deformed at 300°C are stable. It is confirmed by results shown previously using parameter $0 < \eta < 2m$ predicted by (13).

Concluding, there is no instability flow at presented hot deformation conditions in this work.

3.3.3 Comparison Between Atomized and Milled Alloys

3.3.3.1 Flow Stress Behaviour

True stress – true strain behaviour of the atomized and milled samples are significantly different. Sharp peak stress takes place only in milled samples. The behaviour of the atomized samples is typical for 2024 Al alloys when hot compressed at temperature range of 300 to 400°C and strain rate of 0.01 to 1 s⁻¹ (15).

Figure 19 shows true stress – true strain curves of the atomized and milled samples for each temperature and strain rate.

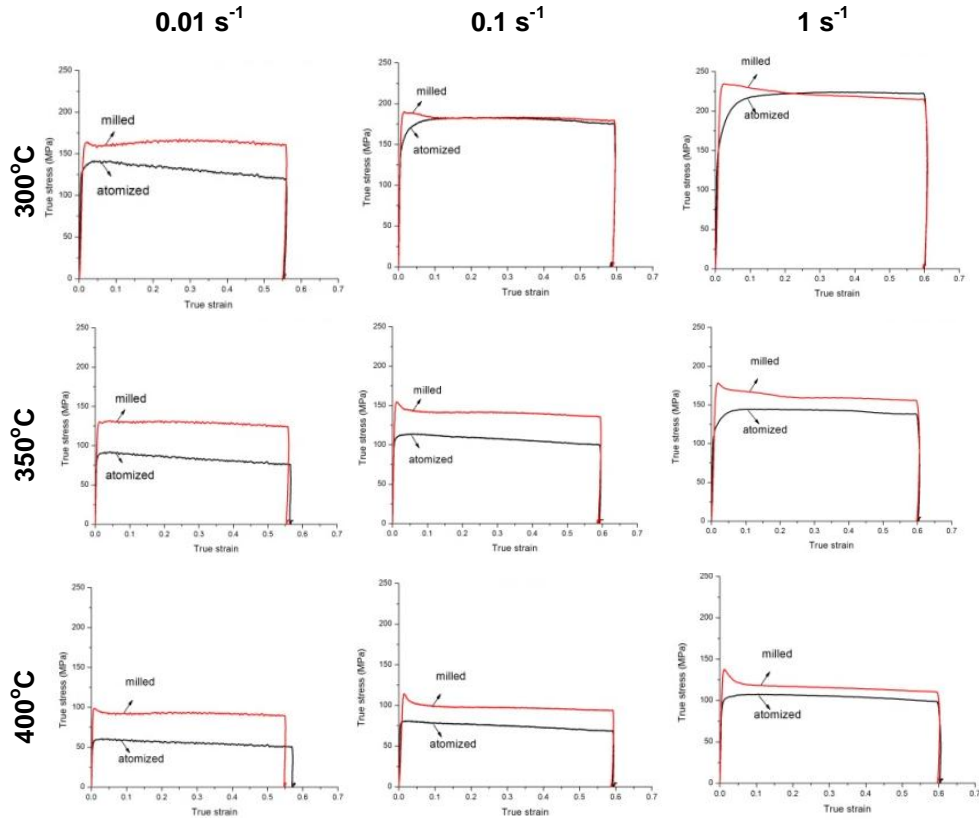


Figure 19: Hot deformation tests of the atomized and milled samples at temperatures of 300, 350 and 400°C with 0.01, 0.1 and 1 s⁻¹ of strain rate.

Flow stress of milled is significantly higher than in case of atomized specimens, except for samples tested at 300°C with 0.1 and 1 s⁻¹ where the curves are overlapped. This significant difference occurs because the flow stress increases with smaller the grain size, as described by Meyers et al. (33). Peak flow stress is always higher in milled samples. The difference of the stress between atomized and milled curves is higher at 0.01 s⁻¹ and diminishes on increases the strain rate.

Figure 20 shows relative work softening of atomized and milled samples at different strain rates.

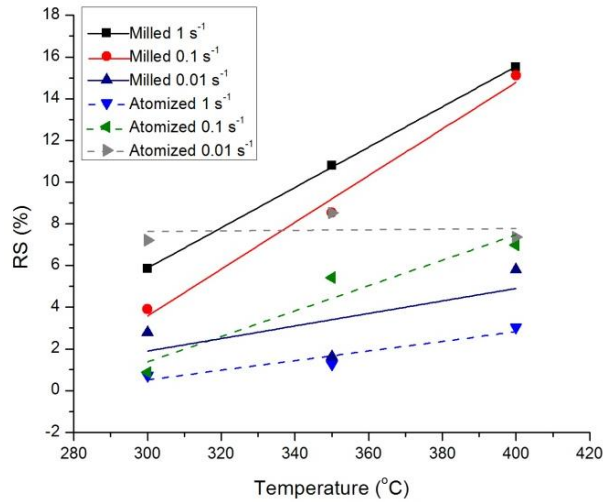


Figure 20: Relative work softening of the atomized and milled samples.

Dashed lines represent atomized samples and solid lines represent milled ones. RS at 0.1 and 1 s⁻¹ of the milled are higher than those related by atomized, considering the slope and the amount of relative work softening. RS of atomized samples at 0.1 and 1 s⁻¹ are correlated to temperature (T) according to the following equations, respectively:

- $RS_{(0.1)} = 0.06T - 16.93$;
- $RS_{(1)} = 0.02T - 6.43$.

Milled samples at 0.01, 0.1 and 1 s⁻¹ follow these equations, respectively:

- $RS_{(0.01)} = 0.03T - 7.11$;
- $RS_{(0.1)} = 0.1T - 30.05$;
- $RS_{(1)} = 0.1T - 23.14$.

It can be seen that the slope of the milled samples is higher than atomized ones.

Figure 21 shows the strain rate sensitivity values of the atomized and milled samples.

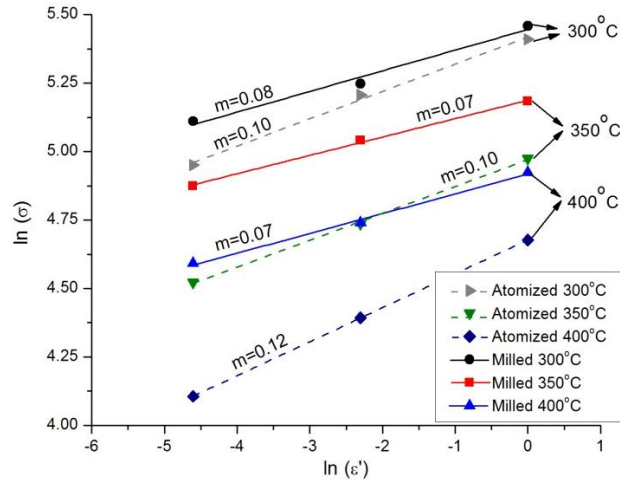


Figure 21: Strain rate sensitivity values of the atomized and milled samples.

The strain rate sensitivity fitted by dashed line represents atomized samples and solid line represents milled specimens. On increasing the temperature the $\ln(\sigma)$ decreases. At the same temperature, milled samples are always positioned over than atomized ones and strain rate sensitivity values display a slightly difference between both samples.

In contrast with the results of this work, some authors (32) (34) have been shown that the strain rate sensitivity for nanocrystalline or UFG are increased in comparison to coarse grained Al and alloys. According to Jafari et al. (32), strain rate sensitivity of 0.01 was obtained for nanostructured 2024 Al alloy and 0.008 for CG 2024 at room temperature. For Al (99.5% of purity), May et al. (34) showed m of 0.25 for UFG Al and of 0.025 for CG Al in compression at 250°C obtained by ECAP.

Table 11 shows efficiency of the atomized and milled samples.

Table 11: Efficiency of atomized and milled samples at three hot deformation temperatures.

	Efficiency (η)		
	300°C	350°C	400°C
Atomized	0.18	0.18	0.21
Milled	0.15	0.13	0.13

As it was seen earlier, the efficiency is in good agreement with literature (15), in which the maximum efficiency is about 29% for 2024 Al alloy when deformed at 380 – 500°C with strain rate of 0.001 – 10 s⁻¹. Since aluminium and alloys are good heat conductor, the low efficiency of samples can be associated to a few microstructural changes and highly adiabatic heating during hot deformation.

Table 12 shows the correlation of workability parameters (m and η) of the atomized and milled samples.

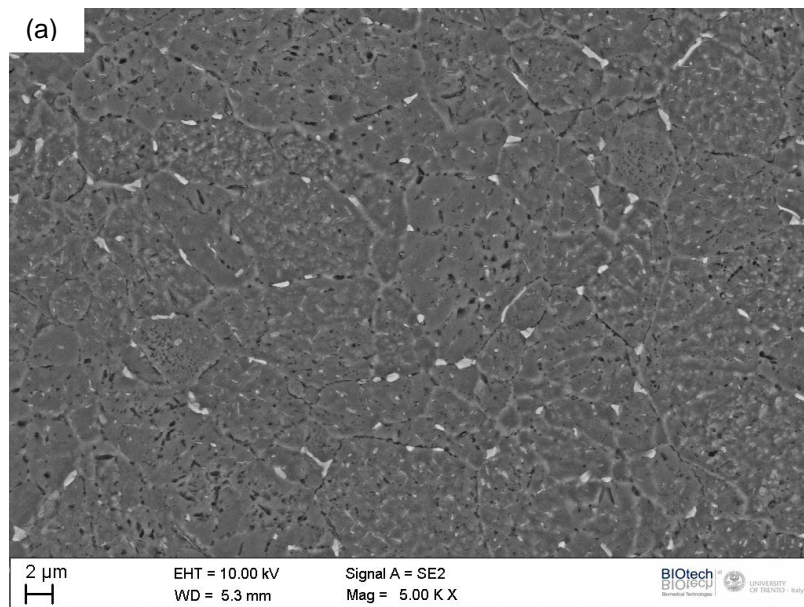
Table 12: Correlation of workability parameters of the atomized and milled samples.

	T (°C)	Workability parameters	
		m	η
Atomized	300	0.10	0.18
	350	0.10	0.18
	400	0.12	0.21
Milled	300	0.08	0.15
	350	0.07	0.13
	400	0.07	0.13

Workability parameters are directly correlated, as expected.

3.3.3.2 Microstructural Characterization

Figure 22 compares SEM microstructure of the atomized and milled samples, respectively.



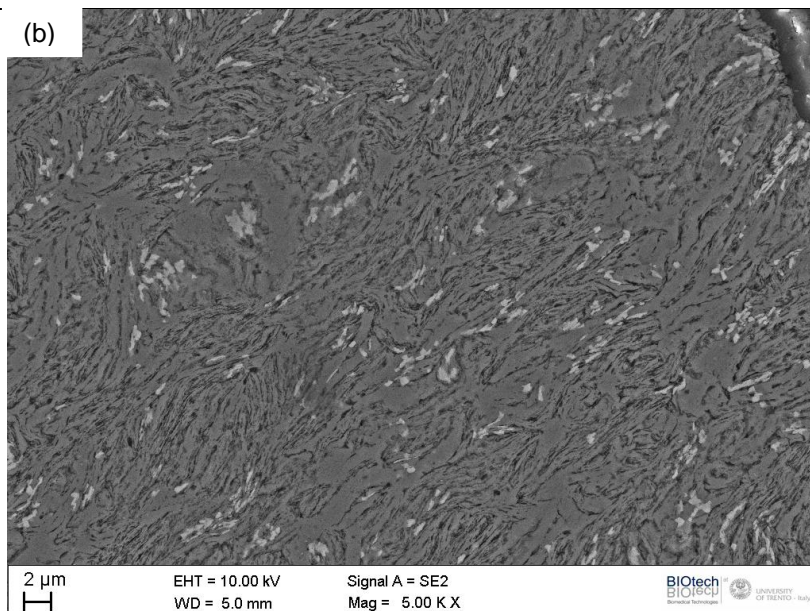


Figure 22: SEM analyses of the (a) atomized and (b) milled materials.

The atomized sample shows equiaxed grains with several homogeneously distributed grain boundary precipitates and fine intragranular precipitates (see Figure 22a). The milled sample shows highly deformed matrix grains and most of the precipitates are agglomerated because of the deformation in milled powder. Residual micropores are also visible.

Figure 23 compares TEM microstructures of the atomized and milled materials.

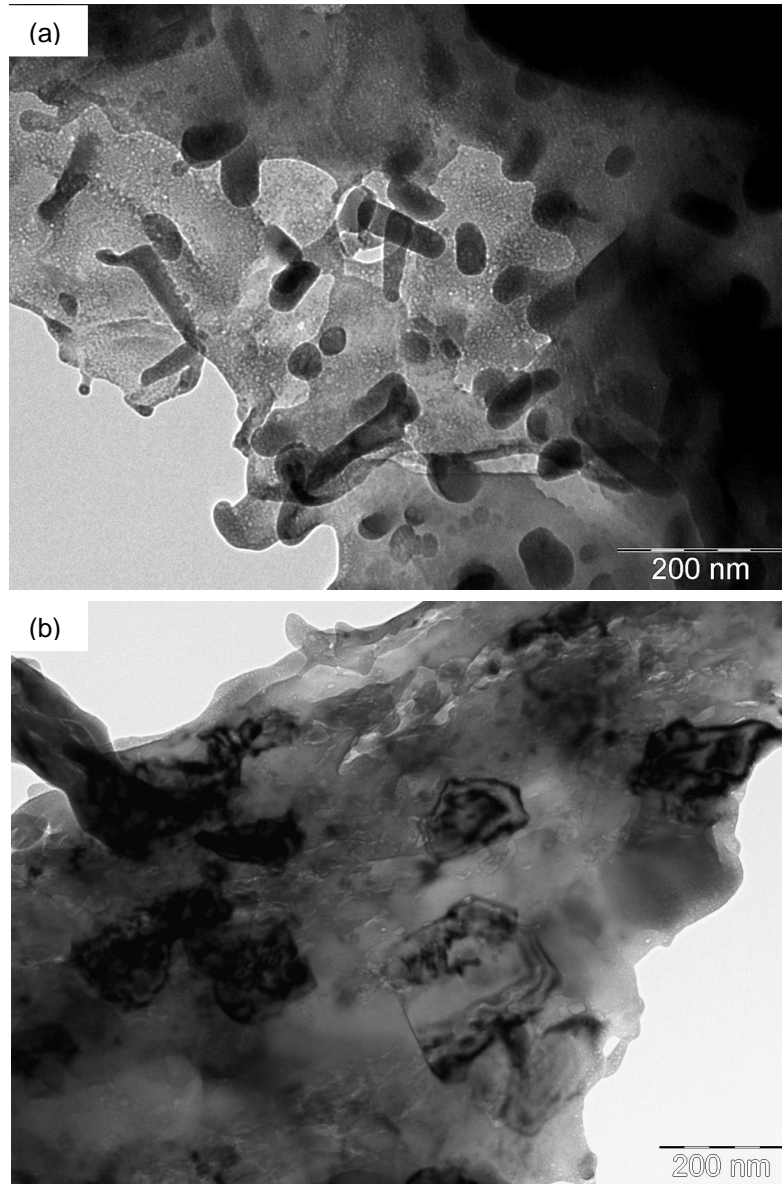


Figure 23: TEM micrographs of (a) atomized and (b) milled materials.

The atomized material (Figure 23a) shows large grains with an extensive precipitation of nanometric θ and S particles (< 100 nm) that are homogeneously dispersed within the microstructure. The milled sample shows finer grains without a significant intragranular precipitation (Figure 23b).

Despite of grain growth during degassing and SPS, the milled material maintains a finer structure than the atomized one. The great difference in the nanometric θ and S precipitation can be justified by considering transformations occurring on degassing and SPS. In the previous chapters it has been shown that transformations on aging are activated by nanostructure and that most of them occur during degassing of the milled powder. Accordingly, the atomized powder is a supersaturated solid solution, whilst the milled and degassed one contains at least the coherent precipitates formed during degassing whose conditions (20h at 250°C) are comparable to typical ageing condition for conventional 2024 Al alloy (3) (35). SPS is carried out at a temperature close to that of the conventional solution annealing treatment but with a very short isothermal soaking time. Therefore it may be hypothesized that:

- in atomized powder, SPS causes the whole of the precipitation sequence, resulting in the extensive intragranular precipitation of incoherent particles;
- in milled and degassed powder, SPS causes the formation of incoherent precipitates and their dissolution in the matrix; not only precipitation, but even solubilization are indeed activated by the large density of structural defects.

Figure 24 shows the TEM images of the atomized and milled samples after hot deformation.

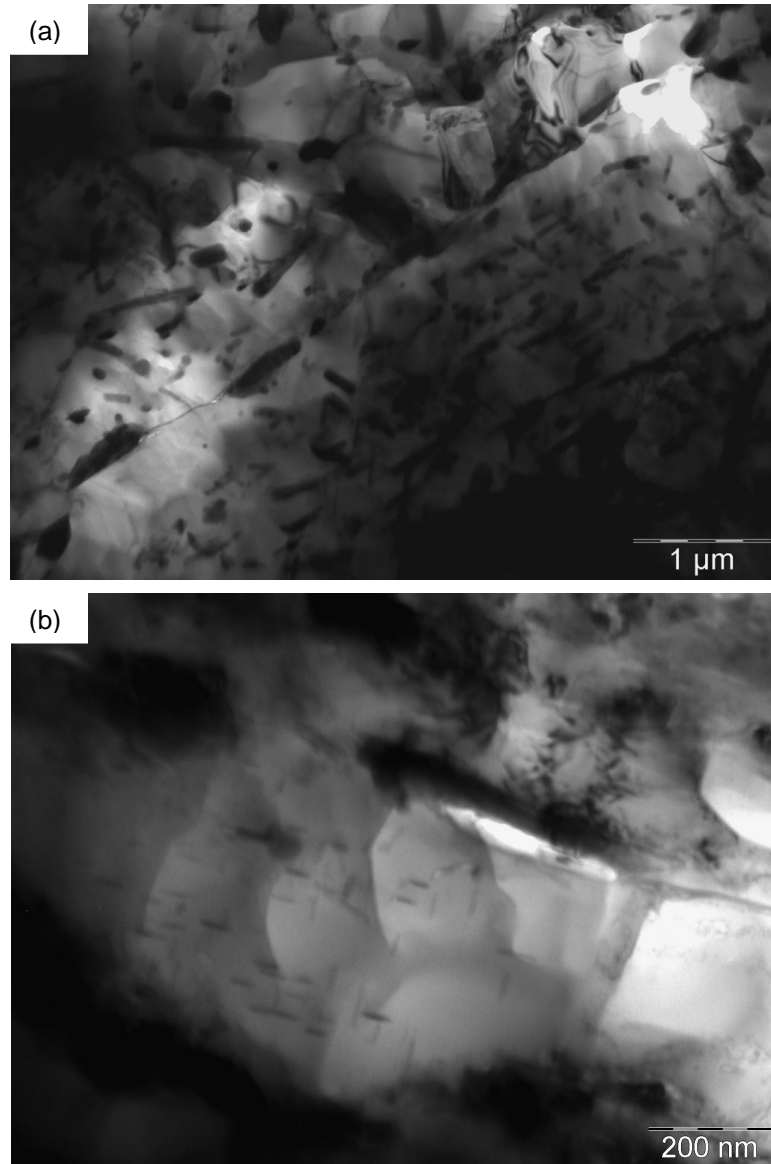


Figure 24: TEM micrographs of (a) atomized and (b) milled samples after hot deformation at 400°C and 0.01s⁻¹.

The atomized sample shows precipitates coarsening after hot deformation (3) (28). They grew from ~ 100 nm to ~ 500 nm maximum (Figure 23a and Figure 24a). The milled alloy presents some small elongated precipitates (< 50 nm), which are nucleated during hot deformation.

The presence of these precipitates may be due to the “deformation-induced nucleation” phenomenon reported by (28), which is responsible of the sharp flow stress peak shown by all the deformation tests of the milled specimens (Figure 10). This precipitation causes a drag stress opposing the motion of dislocations, thus resulting in an increase in the flow stress.

On the basis of the microstructural characterization of the atomized and of the milled specimens, the different hot deformation behavior can therefore be interpreted as follows.

- The sharp flow stress peak of milled specimens is due to the nucleation of precipitates induced by deformation, since the starting microstructure is almost free of intragranular precipitates.
- The higher flow stress of the milled material is due to the finer grain size.
- The slightly lower strain rate sensitivity is likely due to the deformation-induced precipitation.

The last point is not well understood and needs for a further and deep investigation. In the present state of knowledge, a hypothesis can be proposed.

The deformation-induced precipitates cause an increase in flow stress and a slight decrease of the strain rate sensitivity. The drag stress exerted by precipitates can be treated as the effect an internal friction, similarly to that of the Cottrell atmospheres in solution hardening. Drag stress depends on the strain rate; it is zero when strain rate is zero, then it increases with

strain rate up to a maximum and decreases to around zero at very high strain rate. The flow stress of the material is then the sum of two components: the rate-dependent stress (which monotonously increases with strain rate) and the drag stress (which has a maximum at an intermediate strain rate). The two components are shown in Figure 25.

The sum of the two components gives the flow stress.

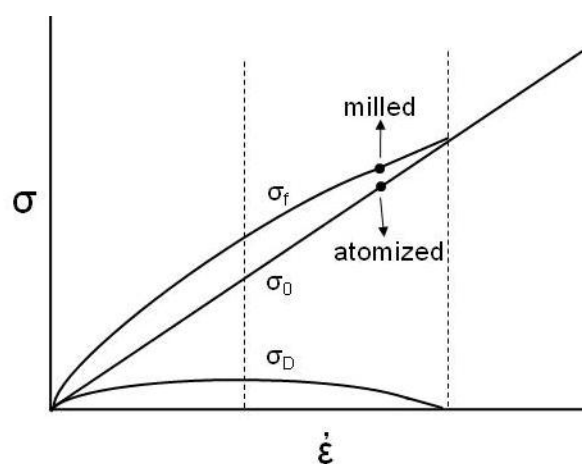


Figure 25: Representation of the flow stress as a function of strain rate for atomized and milled samples.

Whilst the atomized material has the rate-dependent flow stress only, the milled one deforms under the effect of the two components. In the strain rate region indicated in the Figure, the flow stress of the milled material is higher than that of the atomized one, but its strain rate sensitivity is lower. This hypothesis has to be confirmed by a specific investigation.

3.4 Summary

This chapter presents the results of the hot deformation tests of the ultra-fine grained/micrometric 2024 Al alloy. Tests were carried out at different temperatures and strain rates.

The true stress – true strain curves of the milled material presents a decreasing flow stress on increasing temperature and on decreasing strain rate. Flow stress is higher than that of the atomized material in the same conditions, due to the finer grain size. In all the temperature and strain rate conditions, the curves present a sharp flow stress peak, which is not observed in the atomized materials. This peak was attributed to a deformation-induced nucleation of precipitates, which increases the resistance to the motion of dislocations. This precipitation occurs in the milled material only, which has a very poor amount of precipitates in the as sintered condition. Contrarily, the atomized material contains an extensive precipitation of incoherent particles in the as-sintered condition and it does not show the sharp flow stress peak.

The occurrence of such as precipitation in the milled material gives an additional contribution to the increase in the flow stress, with respect to the atomized material.

Strain rate sensitivity of the milled material is slightly lower than that of the atomized material. This could be correlated again to the deformation-induced precipitation, since its effect can be described as that of a drag stress which depends on the strain rate.

The power dissipation efficiency calculation indicates that in all temperature and strain rate conditions investigated the flow is stable, even if efficiency is rather low due to mainly adiabatic heating during hot deformation.

After deformation the milled material maintains the ultra-fine-grained/micrometric structure.

REFERENCES

- (1) N.Jin, H.Zhang, Y.Han, W.Wu, J.Chen. 2009, *Materials Characterization*, Vol. 60, pp. 530-536.
- (2) S.V.S.N.Murty, B.N.Rao. 1998, *Applied Physics*, Vol. 31, pp. 3306-3311.
- (3) X.Huang, H.Zhang, Y.Han, J.Chen. 2010, *Materials Science Engineering A*, Vol. 527, pp. 485-490.
- (4) L.Blaz, E.Evangelista. 1996, *Materials Science and Engineering A*, Vol. 207, pp. 195-201.
- (5) R.Kaibyshev, O.Sitdikov, A.Goloborodko, T.Sakai. 2003, *Materials Science and Engineering A*, Vol. 344, pp. 348-356.
- (6) F.Zhou, X.Z.Liao, Y.T.Zhu, S.Dallek, E.J.Lavernia. 2003, *Acta Materialia*, Vol. 51, pp. 2777–2791.
- (7) L.Jun-peng, S.Jian, Y.Xiao-dong, M.Bai-ping, Y. Liang-ming. 2010, *Transactions of Nonferrous Metals Society of China*, Vol. 20, pp. 189-194.
- (8) R.D.Doherty, D.A.Hughers, F.J.Humphreys, J.J.Jonas, D.J.Jensen, M.E.Kassner, W.E.King, T.R.McNelly, H.J.McQueen, A.D.Rollett. 1997, *Materials Science and Engineering A*, Vol. 239, pp. 219–274.
- (9) M.Rajamuthamilsevan, S.Ramanathan. 2011, *Journal of Alloys and Compounds*, Vol. 509, pp. 948-952.
- (10) E.Evangelista, A.Forcellese, F.Gabrielli, P.Mengucci. 1990, *Journal of Materials Processing Technology*, Vol. 24, pp. 323-332.

- (11) R.Kapoor, J.B.Singh, J.K.Chakravartty. 2008, *Materials Science and Engineering A*, Vol. 496, pp. 308-315.
- (12) A.K.Ghosh. 2007, *Materials Science and Engineering A*, Vol. 463, pp. 36-40.
- (13) S.V.S.N.Murty, B.N.Rao, B.P.Kashyap. 2002, *Journal of Materials Science*, Vol. 37, pp. 1197-1201.
- (14) A.Smolej, B. Skaza, M.Fazarinc. 2009, *Materials and Geoenvironment*, Vol. 56, pp. 389–399.
- (15) Y.V.R.K. Prasad, S.Sasidhara. *Hot Working Guide - A Compendium of Processing Maps*. 1999.
- (16) N.J.Petch. 1953, *Journal of the Iron and Steel Institute*, Vol. 174, pp. 25-28.
- (17) R.A.Masumura, P.M.Hazzledine, C.S.Pande. 1998, *Acta Materialia*, Vol. 46, pp. 4527-4534 .
- (18) B.Zhu, R.J.Asaro, P.Krysl, R.Bailey. 2005, *Acta Materialia*, Vol. 53, pp. 4825–4838.
- (19) S.Cheng, E.Ma, Y.M.Wang, L.J.Kecskes, K.M.Youssef, C.C.Koch, U.P.Trociewitz, K.Han. 2005, *Acta Materialia*, Vol. 53, pp. 1521–1533.
- (20) A.V.Sergueeva, N.A.Mara, A.K.Mukherjee. 2007, *Materials Science and Engineering A* , Vol. 463, pp. 8–13.
- (21) R.J.Asaro, S.Suresh. 2005, *Acta Materialia*, Vol. 53, pp. 3369–3382.
- (22) Q.Weil, S.Cheng, K.T.Ramesh, E.Ma. 2004, *Materials Science and Engineering A*, Vol. 381, pp. 71–79.
- (23) L.Lu, R.Schwaiger, Z.W.Shan, M.Dao, K.Lu, S.Suresh. 2005, *Acta Materialia*, Vol. 53, pp. 2169–2179.
- (24) Y.M.Wang, E.Ma. 2004, *Acta Materialia*, Vol. 52, pp. 1699-1709.
- (25) L.Lu, Y.Shen, X.Chen, K.Lu. 2004, *Science*, Vol. 304, pp. 422–426.

- (26) H.Li, Z.Li, M.Song, X.Liang, F.Guo. 2010, *Materials and Design*, Vol. 31, pp. 2171-2176.
- (27) H.Zhang, G.Y.Lin, D.S.Peng, L.B.Yang, Q.Q.Lin. 2004, *Journal of Materials Processing Technology*, Vol. 148, pp. 245-249.
- (28) G.R.Ebrahimi, A.Zarei-Hanzaki, M.Haghshenas, H.Arabshahi. 2008, *Journal of Mat Processing Technology*, Vol. 206, pp. 25-29.
- (29) I.Charit, R.S.Mishra. 2003, *Materials and Engineering A*, Vol. 359, pp. 290-296.
- (30) T.Seshacharyulu, S.C.Medeiros, W.G.Frazier, Y.V.R.K.Prasad. 2002, *Materials Science and Engineering A*, Vol. 325, pp. 112-125.
- (31) R.W.Hayes, D.Witkin, F.Zhou, E.J.Lavernia. 2004, *Acta Materialia*, Vol. 52, pp. 4259-4271.
- (32) M.Jafari, M.H.Enayati, M.H.Abbasi, F.Karimzadeh. 2010, *Materials and Design*, Vol. 31, pp. 663-669.
- (33) M.A.Meyers, A.Mishra, D.J.Benson. 2006, *Progress in Materials Science*, Vol. 51, pp. 427–556.
- (34) J.May, H.W.Hoppel, M.Goken. 2005, *Scripta Materialia*, Vol. 53, pp. 189-194.
- (35) H.Kaçar, E.Atik, C.Meriç. 2003, *Journal of Materials Processing Technology*, Vol. 142, pp. 762–766.

CONCLUSIONS

In this PhD work, the production of a ultra-fine grained/micrometric Al 2024 alloy by cryomilling and Spark Plasma Sintering, and its deformability at high temperature was studied. The work is divided in three parts: production of the nanostructured powder; consolidation by SPS; hot deformation of the sintered material. The detailed conclusions of the investigation are reported at the end of each chapter. Here the general conclusion remarks are proposed.

A nanostructured 2024 Al powder is obtained by cryomilling with ball-to-powder ratio of 32:1 for 8 hours. Under these conditions a proper compromise between crystallite size and particle size is obtained. On increasing the milling time a further grain refinement is obtained, but particle size becomes too fine for safe handling and “easy” processing. The decrease of the ball-to-powder ratio results in a coarser crystallite size.

Thermal stability of the nanostructured powder is not too high, because of the insufficient lattice strain accumulated during milling. Therefore, grain growth occurs during the degassing treatment (20 hours at 250°C) which has to be carried out before sintering, as usual in aluminium Powder

Conclusions

Metallurgy. The final structure of the degassed powder has a bimodal distribution of grain size in the ultra-fine/micrometric range (1) (2).

A near-full density material can be obtained by SPS at 525°C, 1 minute isothermal holding with a pressure of 60 MPa. The material has an ultra-fine grain structure in range of 100 – 300 nm and micrometric grains. The milled alloy contained θ (Al₂Cu) and S (Al₂CuMg) precipitates in order of 20 – 200 nm, very fine AlN precipitates and grain boundary nanopores. Despite of grain growth occurring on degassing and sintering, the material maintained a structure in the UFG/micrometric range.

The milled material has a higher flow stress and a slightly smaller strain rate sensitivity than the material obtained by sintering the atomized powders. It also presents a sharp flow stress peak, differently from the atomized material. The sharp flow stress peak of milled samples is due to the nucleation of precipitates induced by deformation, since the starting microstructure is almost free of intragranular precipitates. The higher flow stress of the milled material is due to the finer grain size. The slightly lower strain rate sensitivity was likely due to the deformation-induced precipitation.

Processing maps are displayed and they are in good agreement with the literature (3). The flow stress is stable for all conditions studied. The low efficiency was associated to a few microstructural changes and highly adiabatic heating during hot deformation.

REFERENCES

- (1) G.J.Fan, H.Choo, P.K.Liaw, E.J.Lavernia. 2006, *Acta Materialia*, Vol. 54, pp. 1759-1766.
- (2) D.Witkin, Z.Lee, R.Rodriguez, S.Nutt, E.Lavernia. 2003, *Scripta Materialia*, Vol. 49, pp. 297-302.
- (3) Y.V.R.K. Prasad, S.Sasidhara. *Hot Working Guide - A Compendium of Processing Maps*. 1999.

ACKNOWLEDGEMENTS

This research project would not have been possible without the support of the *Fondazione Trentino Universita'* for providing the financial resources, University of Trento, Department of Materials Engineering and Doctoral School in Materials Engineering.

I wish to express my special gratitude to my supervisor, Prof. Dr. Alberto Molinari, who was abundantly helpful and offered invaluable support and guidance.

Special thanks also to all laboratory colleagues, especially to Cinzia Menapace, Nério Vicente Jr., Mario Zadra, Gloria Ischia, Lorena Maines, Angela Berloff, Saliou Diouf, Anna Fredizzi, Elena Santuliana, Ivan Lonardelli, Ibrahim Metinoz, Melania Pilla, Marco Cazzolli and László Lábiscsák for sharing their knowledge, literature and invaluable assistance. Not forgetting to great friends who I met here.

I wish to express my love and gratitude to my beloved family, boyfriend and friends; for their understandings and endless love during my studies.

Finally, I would like to thank God for giving me the opportunity and the strength to perform this study.

PUBLICATIONS

A. MOLINARI, I. LONARDELLI, K. B. DEMETRIO, C. MENAPACE

Effect of the particle size on the thermal stability of nanostructured aluminium powder: dislocation density and second-phase particles controlling the grain growth.

Journal of Materials Science 45 (24) (2010) 6739 - 6746.

K. B. DEMETRIO, I. LONARDELLI, A. MOLINARI

Study of structural features in nanostructured 2024 aluminium alloy obtained by cryomilling and Spark Plasma Sintering.

Proceedings 7th Powder Metallurgy Meeting and 1st International Powder Metallurgy Conference, Porto Alegre (Brazil) 20 - 22 October 2010, p. 47-61.

K. B. DEMETRIO, I. LONARDELLI, C. MENAPACE, A. MOLINARI

Study of the thermal stability and structures features in nanostructured 2024 aluminum alloy obtained by cryomilling.

Proceedings PM2010 World Congress, Florence 10 - 14 October 2010, ed. EPMA, Shrewsbury (UK), 2010, vol. 1, p. 285-292, ISBN 978 1 899072 11 8.

Publications

A. MOLINARI, K. DEMETRIO, I. LONARDELLI, C. MENAPACE, M. ZADRA

Spark Plasma Sintering of nanostructured aluminum powders produced by cryomilling.

Advances in Powder Metallurgy and Particulate Materials 9 (2009) 72 – 78 ISBN: 978-0-9819496-1-1.

I. LONARDELLI, K. B. DEMETRIO, A. MOLINARI

Deformation mechanisms in bulk nanostructured metals: a case study of bimodal grain size distribution.

3rd International Conference on Surface, Coatings and Nanostructured Materials – Barcelona/Spain – 21 - 24 October 2009.

K.B.DEMETRIO, C.MENAPACE, A.MOLINARI

Hot deformation behavior of sub-micrometric 2024 Aluminium alloy during compression at elevated temperature.

International Congress of Mechanical Engineering – Natal/Brazil – 24 – 28 October 2011 (*submitted*).